Intra-cavity light distribution model for photodynamic therapy

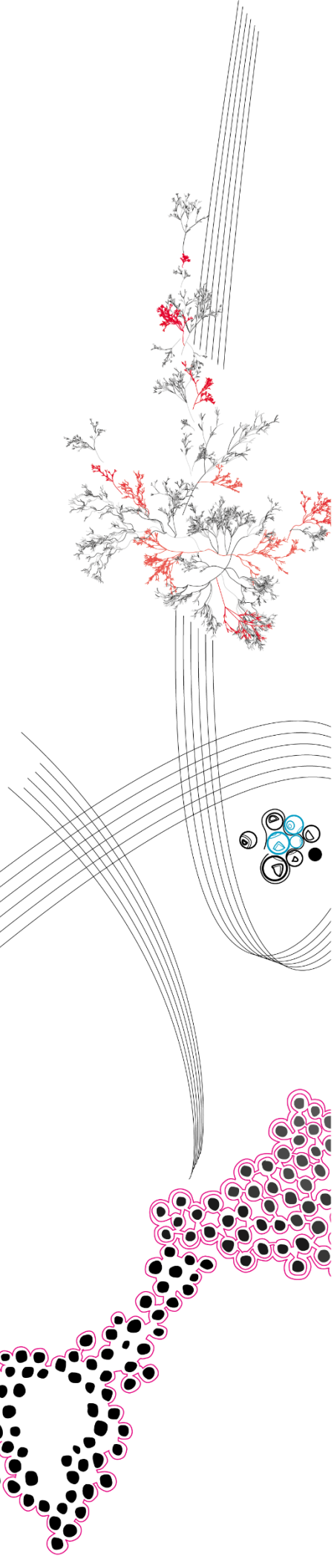

ANTONI VAN LEEUWENHOEK
NEDERLANDS KANKER INSTITUUT

UNIVERSITY OF TWENTE.

Rens Bouwmans
January 2019

Graduation committee:
Chair and technical supervisor
dr.ir. F van der Heijden

Clinical supervisor
dr. M.B. Karakullukçu

Technical supervisors NKI-AVL
dr. ir. R.L.P. van Veen
dr. M.J.A. van Alphen

External member
dr. ir. N. Bosschaart

Process supervisor
drs. R.J. Haarman

Abstract

Introduction. The first steps are made towards a novel approach to improve photodynamic therapy (PDT) used to treat patients with superficial tumors in the sinonasal cavities of the head and neck region. The long-term goal is to improve the efficacy of PDT by improving the planning that is done in advance with the use of an objective planning software tool, which determines the light source location, output power and exposure time. The first steps towards the long-term goal are taken by assessing two possible light distribution models.

Method. An analytic light distribution model was made which is based on radiometric principles and an empiric light distribution model was made based on empiricly found relation between the fluence rate caused by direct initial light and measured fluence rate. Both models were verified with three 3D printed phantom measurements and validated with a tissue phantom measurement.

Results. A cavity specific linear connection was found empiricly between direct initial fluence rate and measured fluence rate. The verification of the models resulted in a root mean square (rms) of 20.8 for the analytic model and 27.5 for the empiric model. The validation of the models resulted in a rms of 8.2 for the analytic model and 7.4 for the empiric model. The analytic model was able to simulate all measured fluence rates whereas the empiric model was able to simulate only the fluence rates measured by the measuring probes that received direct initial light.

Conclusion. Both models showed acceptable simulations within the conducted phantom measurements. Regarding the clinically applicability and the calculation speed it seems that the empiric model is more clinically applicable than the analytic model, however more research is needed to give a definitive conclusion on this.

List of abbreviations

3DPP	three dimensional printed phantoms
ABS	acrylonitrile butadiene styrene
$\boldsymbol{\beta}$	build-up factor
$\boldsymbol{\beta(r)}$	build-up function
cPDT	cavity photodynamic therapy
CT	computed tomography
HNSCC	head and neck squamous cell cancer
MC	Monte Carlo
OR	operating room
PDT	photodynamic therapy
PS	photosensitizer
$\boldsymbol{R_d}$	diffuse reflection coefficient
rms	root mean square
ROS	reactive oxygen species
TP	tissue phantom

Contents

1. Introduction

This thesis describes the first steps in the development of a novel approach to improve photodynamic therapy (PDT) used to treat patients with superficial tumors in the sinonasal cavities of the head and neck region. PDT in cavities is revered to as cavity PDT (cPDT) and is used to e.g. treat residual superficial tumors in the sinonasal cavity (Figure 1). The first steps towards a light dosimetry planning tool are made, which will assist the surgeon with the optimal positioning and output power of the laser light source.

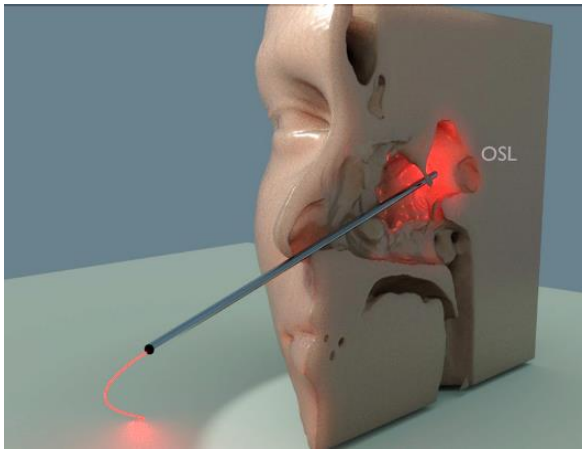

Figure 1 - A raytracing rendered impression of a sinus cPDT illumination (Sagittal cross-section of the Head) The metal tube represents an EM navigation pointer to which a PDT light source is connected

1.1. Head and neck tumors

The conventional treatments of head and neck tumors consists of surgery, (chemo)radiotherapy and the combination of both.[1] In the Netherlands about 3081 new cases of these head and neck tumors where diagnosed in 2017 of which the majority is classified as head and neck squamous cell cancers (HNSCC).[2,3] Fifty percent of the patients fail first line of treatment. Successive salvage surgery provides around 35% 5-year survival and is often complex with functional losses and impaired wound healing. Re-radiation is often not possible due to the increased radiotoxicity of vital structures. An alternative would be chemoradiation, however the patient needs to be in a good health condition which is often not the case.[3] If the conventional treatments are exhausted, cPDT is used as a treatment for HNSCCs to increase the quality of life and curative in case of superficial tumors in the oral cavity.[3–8]

1.2. Photodynamic therapy

PDT is a local minimally invasive treatment for superficial (pre-)malignant lesions and advanced or recurrent malignancies. It does not limit future treatment options and can be repeated without losing its efficacy.[3,6,7] The therapy consists of three components (photosensitizer (PS), light of specific wavelength and oxygen), which in combination and in the right concentration create multiple reactions that generate reactive oxygen species that in turn induce cell necrosis, apoptosis and/or autophagy.[7,9–12] Of the three components light delivery is adjustable during procedure, whereas PS administration is established in protocols and oxygen supply is tissue dependent.[13] Light delivery can be described in light dose (ψ in J/cm^2) and fluence rate (φ in mW/cm^2), which have an empiric determined optimal value of respectively 20 J/cm^2 and 100 mW/cm^2 for the photosensitizer Foscan™.[8,14] In the event of insufficient light, the PDT effect might be unsatisfactory while in the case of too much light oxygen depletion will take place with reduction of the efficacy.[15] Thus optimal light distribution is needed which illuminates the tumor tissue enough to induce cell death and illuminates healthy tissue as little as possible to prevent tissue damage.[16,17]

Achieving an optimal light dose distribution for cPDT in a complex geometry i.e. paranasal sinuses or its defect after surgery with varying optical properties of tissue makes correct light delivery challenging.[18] Whereas the optical properties can even change during procedure, making correct light delivery even harder.[3,13,19,20]

A plan is made to achieve a good light dose distribution, which includes light source positioning, light source type, laser output and exposure time. Currently the planning is done first orderly by scrolling the 2D (sagittal, coronal and transverse planes) images of the CT to intuitively determine the best light source position, type, output power and exposure time. Then the source location is marked in the CT DICOM files so that the surgeon can maneuver and fixate the light source to the pre-determined position via electromagnetic navigation. This current method of planning gives a rough estimation of the optimal light source location, output power and exposure time. However, it lacks precision, accuracy and does not take tissue backscattering into account as it is based on intuition and no physical modelling.

1.3. Long-term goal

The long-term goal is to improve the efficacy of PDT by improving the planning that is done in advance. This planning should ideally be no longer based on intuition but on physical calculations, creating a higher degree of accuracy and ensuring limited operator-dependency. A planning software tool would be the goal which enables the operator to plan an optimal light source position, type, output power and exposure time based on a light distribution model. Practically this would mean that the software tool calculates light source location(s), output power(s) and exposure time(s) that will ensure the most ideal light distribution, based on mathematical calculations.

1.4. Research question

A calculated-based instead of intuition-based planning is thus desirable, but the question remains what algorithm ideally should be used for this planning software tool. The first steps towards the long-term goal are taken by assessing possible light distribution models.

Light distribution simulations are already available, such as Monte Carlo (MC) simulations and approximations of the diffusion theory. MC simulations are very accurate, but time-consuming and impractical. They require detailed knowledge of the optical properties and require large computation times which makes them not suitable for optimization as the simulations needs to be repeated multiple times.[21–23] Approximations of the diffusion theory have been investigated which calculate the initial light fall and add a constant that represents the scattered light.[16] However this simulation is a rough estimation and may not take into account the patient specific cavity geometry and its accompanying reflectance pattern. So, both light distribution models have their own drawbacks with regards to be clinical applicability for optimal source planning.

Two new light distribution models will be designed, one based on radiometric principles and the other based on an empiricly conceived entity, the build-up factor β, obtained in earlier performed measurements by T. van Doeveren and R. van Veen. The aim is to develop a simple, reliable and fast model that can be used in optimization algorithms. An accuracy of approximately +/- 20 mW is aimed for and the calculation time should be kept to a minimum and not exceed more than half a minute. Both models will be evaluated and compared to determine the best possible light distribution model.

There are a lot of light delivery systems e.g. cylindrical diffusors, spherical diffusors, micro-lenses, applicators, etc. however in the first attempt we assume that light will be delivered with spherical fibers because of its simplicity.[21,24]

1.5. Outline of thesis

The outline of this thesis to address the described research question is visualized in Figure 2 and consists of four consecutive parts: an analytic approach, empiric approach, verification and validation of the models.

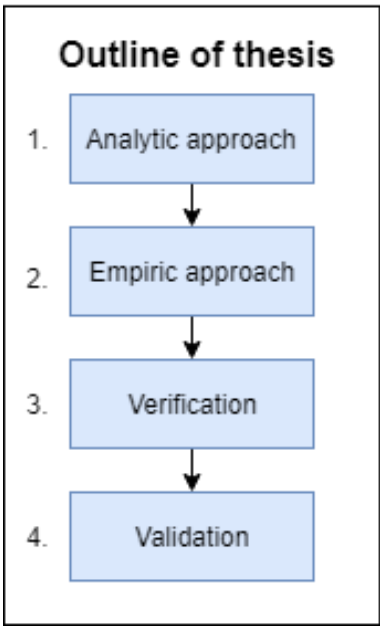

Figure 2 - Schematic visualization of the outline of the thesis.

The first step is creating an analytic light distribution model which is based on radiometric principles. It will subtract the surface of the cavity wall from the CT scans and perform simulations with the assumption that the cavity wall is a Lambertian surface.

The second step includes light dosimetry measurements and the development of the empiric light distribution model. To gain more detailed insight on how light is distributed, 3D printed patient specific models (3DPP) were developed. These models allow for more surface measurements in cavity regions that are not accessible in in-vivo measurements during cPDT. These models have homogenously distributed optical properties; absorption μ_a and scattering μ_s, because they are printed in one material. The light distribution therefore solely depends on the geometry of the cavity. From these models we can determine the contribution of light scattering throughout the irregular shaped cavity. From these phantom measurements an empiric light distribution model is expected to be derived.

Third step is the verification of the models in which the developed light distribution models will be used to simulate the fluence rates in the 3DPPs which are used in the measurements in the previous step.

The last step is the validation of the models with the use of a tissue phantom measurement. Light distribution within a hollow structure is also dependent on the light absorbing ability of the wall.[17,25] The created tissue phantom (TP) is therefore a step closer towards the optical properties of tissue in clinical practice. This phantom is assumed to give more insight in the light distribution and the feasibility of the simulation models as it is made of tissue.

2. Background

2.1. PDT mechanism

PDT consists of three components i.e. photosensitizer, light and oxygen which individually are harmless components but induce a photodynamic effect when combined.[7,10,26] When the photosensitizer is exposed to light corresponding to its absorbance band it becomes energized and moves from a ground state to an excited state (Figure 3).[7,10] This reactive form loses its energy by interacting with oxygen in two ways, type I and type II, leading to the creation of respectively reactive oxygen species (ROS) and singlet oxygen.[26]

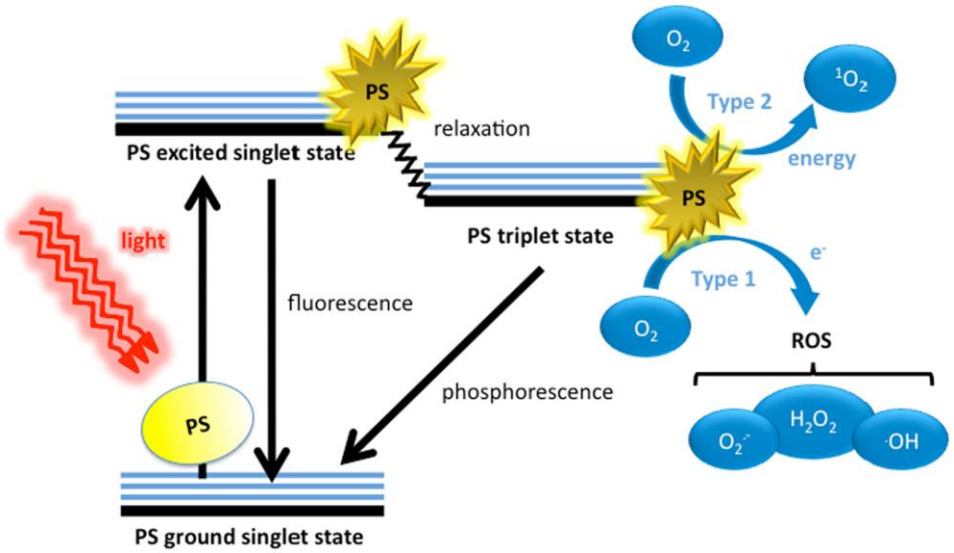

Figure 3 - Schematic illustration of photodynamic therapy. The PS initially absorbs light corresponding to its absorbance band that excites it to the first excited singlet state. It can then relax to the more long-lived triplet state. In the presence of oxygen this triplet PS form reactive oxygen species (ROS) and singlet oxygen via type I and type II pathways respectively.[26,27]

Three main mechanisms exist in which the created products of oxidation can mediate tumor destruction. The first mechanism is the direct attack on tumor cells, whereas it can also attack cells that make up the blood supply of the tumor which is the second mechanism. The final mechanism is the activation of the immune system against the tumor.[3,9,10]

2.2. Radiometric basics of tissue optics

2.2.1. Direct incident illumination

In PDT light is delivered to the region of interest via optical quarts fibers. At the distal end of the fiber there can be a miniature spherical diffusor, cylindrical diffusor or a micro-lens. In our experiments we used the spherical diffuser or a micro-lens (Figure 4).

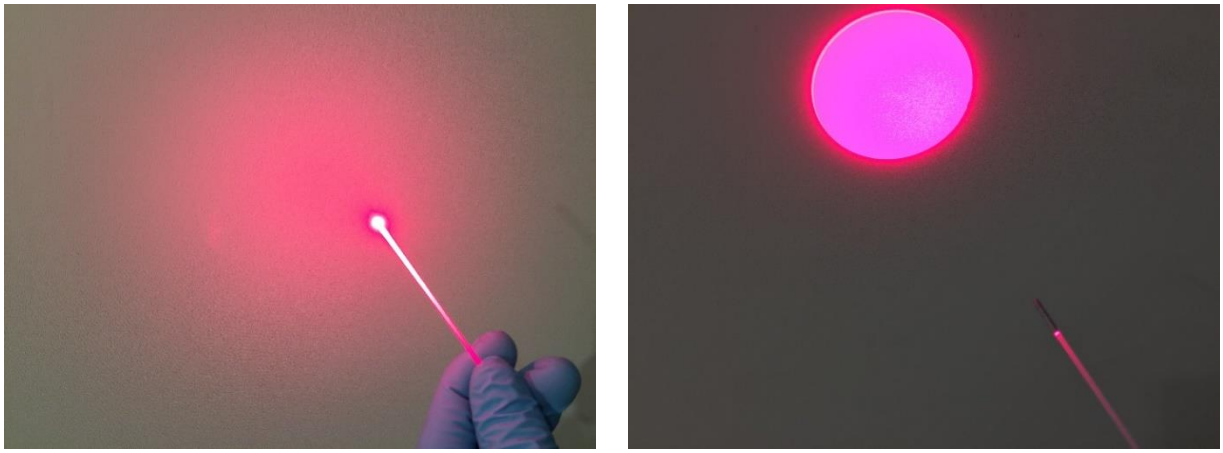

Figure 4 - Two different optical quarts fiber tips were utilized. Left is the spherical diffusor (Medlight SA, Ecublens, Switzerland) visualized emitting light diffusively and right the micro-lens (Medlight SA, Ecublens, Switzerland) emitting a spot of light.

Light is emitted into the sinonasal cavity with the use of these light sources, creating an illumination of the cavity. Photons travel from the source towards the wall of the cavity and interacts for the first time with tissue. This light is called direct incident light and can be described in incident fluence rate (φ_{inc} in mW/cm^2). Other areas form shadow areas, they do not receive direct initial light from the source (Figure 5).

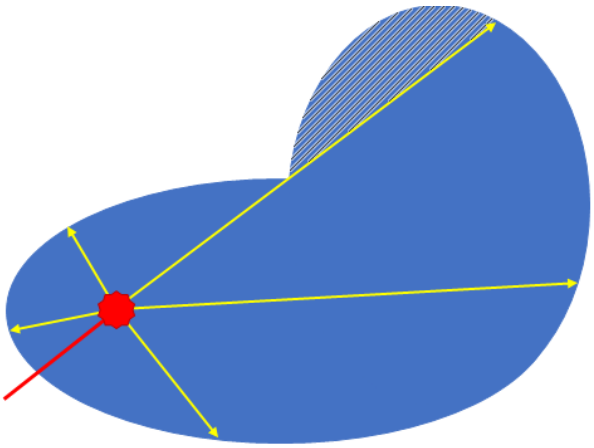

Figure 5 - Schematic 2D visualization of illumination of a surface within a cavity (blue). A spherical light diffusor is marked with a red dot and 5 possible light rays are indicated with yellow arrows. The wall of the cavity is fully illuminated except in the striped area.

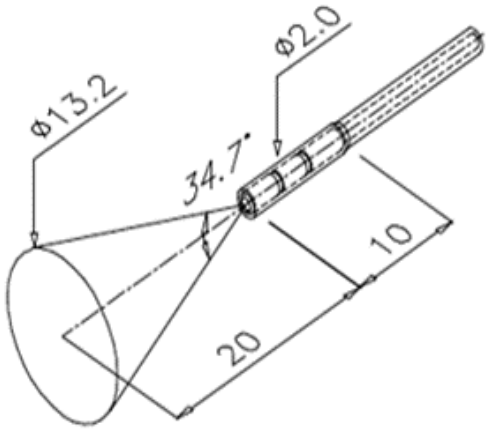

Figure 6 - Schematic representation of the micro-lens and the spot it creates.

In case the light source is a spherical diffuser with a known laser output power P_{out} and distance between source and surface r, the incidence fluence rate can be calculated with equation (1). The incidence fluence rate is the same as the irradiance on the surface created directly by the light source.

$$\varphi_{inc,diffuser} = \frac{P_{out}}{4\pi r^2} \quad (1)$$

In case of a micro-lens (Figure 4) calculation of the incident fluence rate is different. The micro-lens is designed to homogeneously illuminate a spot as is shown in Figure 6. The incident fluence rate is for every position in this spot the same and can be calculated with equation (2):

$$\varphi_{inc,lens} = \frac{P_{out}}{surface\ area\ spot} = \frac{P_{out}}{\pi(tan(17{,}35°)r)^2} \quad (2)$$

where the $tan\ (17.35°)$ *factor in the denominator describes the fixed angle of the micro-lens i.e. numerical aperture, that is used.*

2.2.2.Scatter illumination

When light reaches the surface of the tissue, it interacts with it in a certain way depending on the optical properties of the tissue. An overview of all the possible interactions of light is visualized in Figure 7. One optical property of tissue is the scattering which is the ability to alter the direction of a propagating wave. It is described with the scatter coefficient μ_s which is the probability of scattering per unit distance.[25] Another optical property of tissue is the ability to absorb light. This property is called the absorption coefficient μ_a, which is the probability of absorption per unit distance.[25] A part of the light will thus be reflected, scattered or absorbed, whereas the scattering dominates in the red and near infrared spectrum.[28]

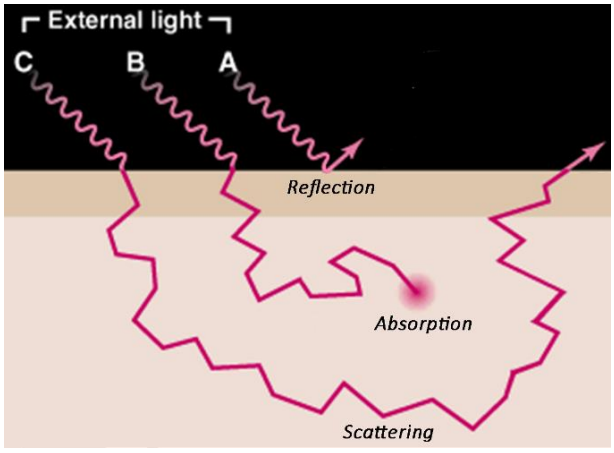

Figure 7 - Light-tissue interaction. (modified from Benaron et al.) Some photons are directly reflected by the surface of the tissue (A) Other photons are absorbed by the tissue (B). And other photons follow a random path due to scattering events (C).

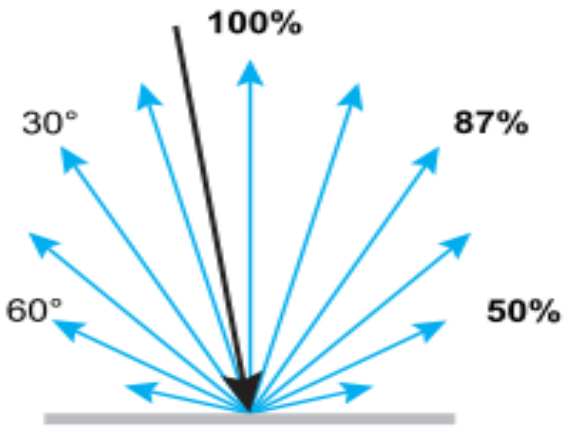

Figure 8 - Lambertian distribution of light on a Lambertian surface.

In this thesis the assumption is made that that the wall of the cavity diffusely scatters light back (back scatter) into the cavity according to Lambert's cosine law. Multiple studies made the same assumption and justified this assumption.[29–31] Lambert's cosine law of diffuse reflection describes the reflectance of an ideal diffuse reflecting surface, this reflectance is called Lambertian reflectance. A surface possessing this Lambertian reflectance is ideal 'matte' and its brightness (luminance) appears to be the same for the observer regardless the angle of observation. The radiant intensity (*W/sr*) emitted by a point on a Lambertian surface is described with the following equation:

$$I(\theta) = I_{\max}\cos(\theta) \quad (3)$$

where I_{max} is the maximum radiant intensity (W/sr) and θ is the emission angle.

$I_{\max}$ is the intensity emitted along the vertical axis and I(θ) is the intensity emitted at an angle θ. It is not a point that emits light back into the cavity, but it is a small surface. For small surfaces and described in radiometric quantities the re-emittance of a Lambertian surface is described with the equation:

$$I(\theta) = Lcos(\theta)A \quad (4)$$

where L is the radiant intensity per foreshortened area (W/m^{2}sr) and A (m^2) the area of the surface.[32]

A large proportion of the incident light is diffusely re-emitted at the tissue surface into the cavity and may re-enter tissue somewhere else in case of hollow structures like the sinonasal cavity. The amount of re-emitted light (back scatter) depends on the optical properties of the tissue.[29,33]

2.2.3. Fluence rate build-up factor

The total fluence rate φ_{total} at the surface is the sum of the incident fluence rate φ_{inc} and the scatter fluence rate $\varphi_{scatter}$ (equation (5) & Figure 9). It is a measure for the amount of light available for photosensitizer absorption.[17]

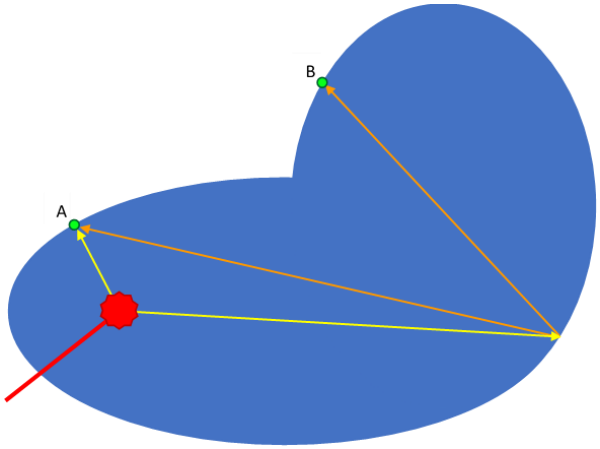

Figure 9 - Schematic visualization of the total fluence rate at two points in a cavity. Point A is directly illuminated and receives incident light fluence and scattered fluence, whereas point an only receives scattered fluence. In this schematic visualization only one point is drawn that scatters light, but in reality, all points on the wall re-emit light back into the cavity.

$$\varphi_{total} = \varphi_{inc} + \varphi_{scatter} \quad (5)$$

The fluence rate at the surface of the cavity is composed of direct incident light and scattered light. The latter consists of photons traveling toward the surface and photon that are re-emitted at the surface i.e. diffuse reflectance.

The scatter fluence rate $\varphi_{scatter}$ describes the fluence rate at the surface which is scattered and reflected by the cavity wall. The incidence fluence rate φ_{inc} describes the non-scattered fluence rate at the surface due to direct incident light.

The ratio between the fluence rate at the surface of the cavity and the incident fluence rate is the build-up factor β which can be calculated with the following equation:

$$\beta = \varphi_{total}/\varphi_{inc} \quad (6)$$

Combining this equation with the given incident fluence rate equations for a spherical diffusor (1) and micro-lens (2) will give us respectively the equations (7) and (8).

$$\beta_{diffusor} = \frac{\varphi_{total} 4\pi r^2}{P_{out}} \tag{7}$$

$$\beta_{lens} = \frac{\varphi_{total} \pi (tan(17{,}35°) r)^2}{P_{out}} \tag{8}$$

3. Materials and Methods

3.1. Analytic approach

3.1.1. Cavity wall

The cavity wall that will be illuminated was subtracted from CT images. The first step was to load the DICOM into MATLAB and resize the image to ensure isotropic pixels. The information needed for resizing was gathered from the DICOM-info. Then the image was manually cropped. The volume size of the cropped image was kept to a minimum to limit further unnecessary computations. The cropped image should at least contain the whole cavity that would be illuminated along with the connected cavities to simulate light distribution properly.

The cavity wall was a surface which was located at the edge between air and tissue, therefore a distinction needs to be made between air and tissue. A threshold was applied to create a binary image which distinguishes tissue from air. Now this image contained all the aerial volumes within the cropped area. These aerial volumes were often connected with the air outside the head e.g. via nostrils. A mask was applied to remove the aerial volumes outside the head and select only aerial volumes within the head. The location of the light source was then manually selected. This location also selected the correct aerial volume in the binary cropped image.

The surface of this selected aerial volume was then be made with the MATLAB command ‘isosurface’ using an iso value of 0. The created surface was made of small triangles i.e. faces which all had three vertices (Figure 10). The amount of faces was reduced with the function ‘reducepatch’ to ensure lighter calculations while preserving the shape as much as possible.

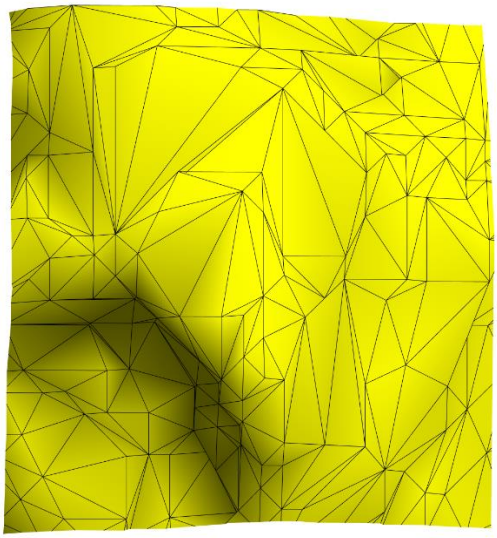

Figure 10 - Surface sample of cavity wall created with the 'isosurface' and ‘reducepatch’ command in MATLAB. This surface was made of multiple small triangles i.e. faces which differ in size. The dark area in the lower left corner represent shadow, indicating the 3D feature of the surface. The yellow color was chosen arbitrarily.

3.1.2. Direct incident Light

Calculations of the direct incident light fall are described based on a simplified example of one face. A schematic overview of the situation is drawn in Figure 11. The known parameters are the coordinates of the source S and the coordinates of vertices P, Q and R that make up the face.

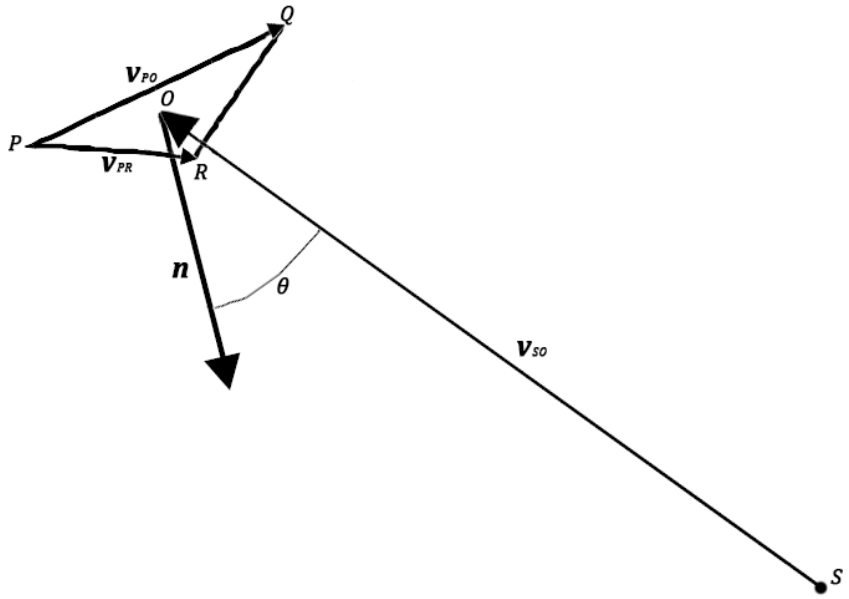

Figure 11 - Schematic representation of face PQR receiving light from a light source S and the geometrical properties used for irradiance calculation. $\boldsymbol{v}_{SO}$ is a vector between point S and the center of the face O. $\boldsymbol{v}_{PQ}$ and $\boldsymbol{v}_{PR}$ are vectors from vertex P to respectively vertices Q and R. $\boldsymbol{n}$ is the normal vector of the face originating in O and the angle of incidence θ is the angle between $\boldsymbol{n}$ and $\boldsymbol{v}_{SO}$.

First the coordinates of the center point of the face O were calculated with the following equations:

$$O_x = \frac{P_x+Q_x+R_x}{3} \qquad O_y = \frac{P_y+Q_y+R_y}{3} \qquad O_z = \frac{P_z+Q_z+R_z}{3} \tag{9}$$

where O_x, O_y and O_z are respectively the x, y and z coordinates of O. The same is true for vertices P, Q and R.

A vector $\boldsymbol{v}_{SO}$ was then created between the points S and O which was calculated with the following equation:

$$\boldsymbol{v}_{SO} = \left(S_x - O_x\,, S_y - O_y\,, S_z - O_z\right) \tag{10}$$

$\boldsymbol{v}_{PQ}$ and $\boldsymbol{v}_{PR}$ are vectors from vertex P to respectively vertex Q and R. They are determined the same way as vector $\boldsymbol{v}_{SO}$. These vectors are used to determine the normal $\boldsymbol{n}$ vector of the area with the cross product:

$$\boldsymbol{n} = \boldsymbol{v}_{PQ} \times \boldsymbol{v}_{PR} \tag{11}$$

The angle of incidence was determined by calculating the angle between vector $\boldsymbol{v}_{SO}$ and the normal vector of the face $\boldsymbol{n}$. This was done with the use of the unit vectors of both vectors:

$$\cos(\theta) = \widehat{\boldsymbol{v}_{SO}} \cdot \hat{\boldsymbol{n}} \tag{12}$$

where $\widehat{\boldsymbol{v}_{SO}}$ is the unit vector of $\boldsymbol{v}_{SO}$ and $\hat{\boldsymbol{n}}$ the unit vector of $\boldsymbol{n}$.

To check whether shadow was cast on the face three vectors ($\boldsymbol{v}_{SP}$, $\boldsymbol{v}_{SQ}$, $\boldsymbol{v}_{SR}$) were created running from the source toward the three vertices (Figure 12). Along these vectors it was checked if they cross non-aerial voxels e.g. tissue. A value of zero will be addressed to the vectors that cross tissue voxels and a value of one to those that do only cross aerial voxels. The mean of these values represents a fraction f a face was illuminated by direct incident light, which could adapt the values 0, $^1/_3$, $^2/_3$ or 1.

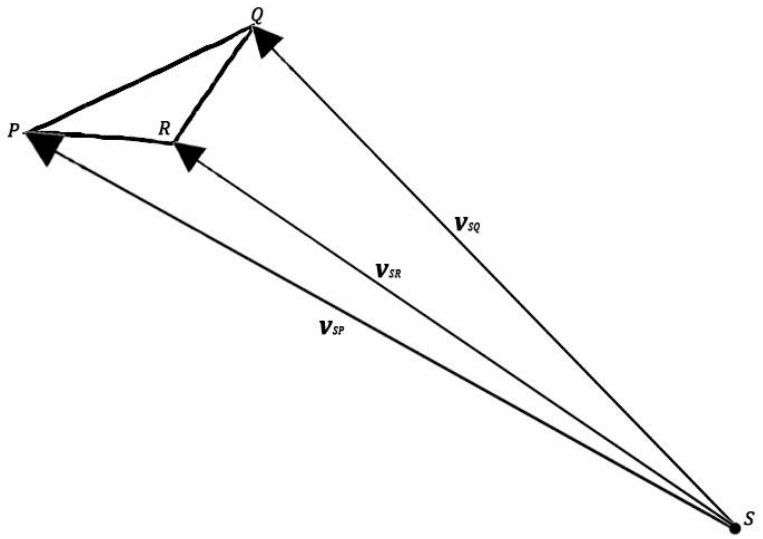

Figure 12 - Schematic representation of face PQR and vectors $\boldsymbol{v}_{SP}$, $\boldsymbol{v}_{SQ}$ and $\boldsymbol{v}_{SR}$ drawn from point S towards the vertices P, Q and R respectively.

The irradiance on the face was then calculated as follows:

$$E_{direct} = \frac{P_{out}\cos(\theta)}{4\pi\|\boldsymbol{v}_{SO}\|^2} f_{direct} \tag{13}$$

where E_{direct} is the irradiance due to direct incident light, $\|\boldsymbol{v}_{SO}\|$ the magnitude of vector $\boldsymbol{v}_{SO}$ and f_{direct} the fraction of blocked initial light on the face.

The surface area of the face (A) was used to calculate the radiant flux on the face. The surface area is:

$$A = \frac{\|\boldsymbol{n}\|}{2} \tag{14}$$

where $\|\boldsymbol{n}\|$ is the magnitude of $\boldsymbol{n}$.

The radiant flux on the face was calculated by multiplying the irradiance on the face with the surface area of the face:

$$\phi = EA \tag{15}$$

where E is the irradiance on the face and A is the area of the face.

3.1.3. Diffuse re-emittance

Tissue receives an amount of energy which it will absorb, reflect and scatter. In this model the percentage of received energy that it will send back into the cavity was indicated with the diffuse reflection coefficient

(R_d). Re-emittance of light is assumed to obey Lamberts law of diffuse reflection which is described briefly in the background section. Calculations of the backscattering is further explained based on a simplified situation of two faces (Figure 13).

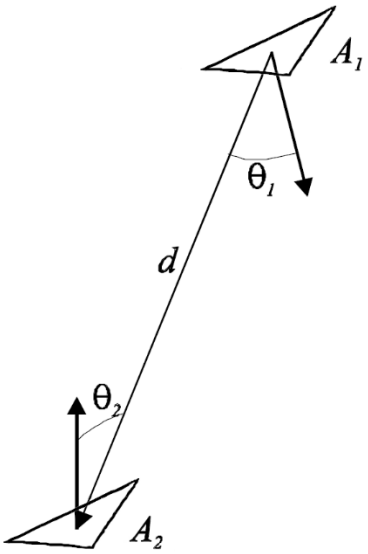

Figure 13 - Schematic representation of a reflecting face (A_1) and a receiving face (A_2) which are separated with a distance d. θ_1 and θ_2 are the angles between vector between the centroids of A_1 and A_2 and their corresponding normal vectors.

In case of a Lambertian surface the irradiance of a reflecting face onto a receiving face is described as[32]:

$$E_2 = \frac{L\cos(\theta_1)\cos(\theta_2)\,A_1}{d^2} f_{diffuse} \tag{16}$$

where E_2 is the irradiance on the receiving face from the reflecting face (W/m^2), L the radiance of the reflecting face (W/m^{2}sr), A_1 the surface area of the reflecting face (m^2) and $f_{diffuse}$ the fraction of light blocked from the reflecting face on the receiving face. θ_1 is the emittance angle and θ_2 is the angle of incidence.

The total exitance of a Lambertian radiator is the radiant flux from a surface which can be calculated with:

$$M = \pi L \tag{17}$$

where M the total exitance of the face (W/m^2) is.

The radiant flux of the reflecting face equals:

$$M = R_d E_1 \tag{18}$$

where E_1 the total irradiance the face received (W/m^2).

Combining equations (16) with equations (17) and (18) result in equation:

$$E_2 = \frac{R_d E_1 cos(\theta_1)\cos(\theta_2)\,A_1}{\pi \|\boldsymbol{v}_{SO}\|^2} f_{diffuse} \tag{19}$$

The calculations above were done for all the face combinations. Thus, the irradiance on a single face is the sum of the irradiances it receives from all other faces Figure 14 and equation (20).

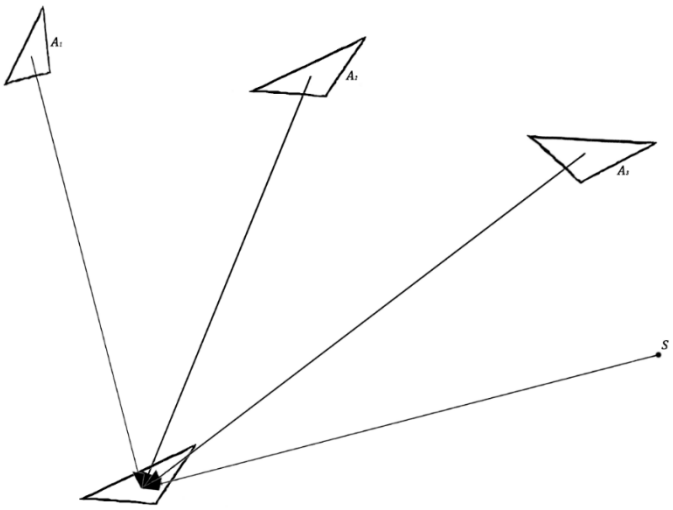

Figure 14 - The total irradiance a face receives is the sum of all the individual irradiances it receives from other faces and the direct incident irradiance from the light source S.

Multiple reflections were simulated by repeating the above described equations. Thus, energy will travel from light source to the first face, towards the second, towards the third, etc.

$$E_{face,total} = E_{direct} + \sum_{j=1}^{n}\sum_{k=1}^{m} E_{j,k} \tag{20}$$

where n represents the number of reflections simulated and m is the total amount of faces the cavity is made of.

The fluence rate per face after multiple reflections can be calculated with the use of the irradiancy on a single face after multiple reflections with the following equation:

$$\varphi_{face,total} = (1 + R_d)E_{face,total} \tag{21}$$

This equation, thus the link between irradiance and fluence rate is explained in Figure 15, in which a measuring probe is visualized just above a surface. This measuring probe measures fluence rates. The light source emits light which will create irradiance on the surface. This surface also reflects a portion of the received irradiance which is also detected by the probe. Thus, the measured fluence is a summation of the irradiance on a surface and the portion that is reflected by the surface.

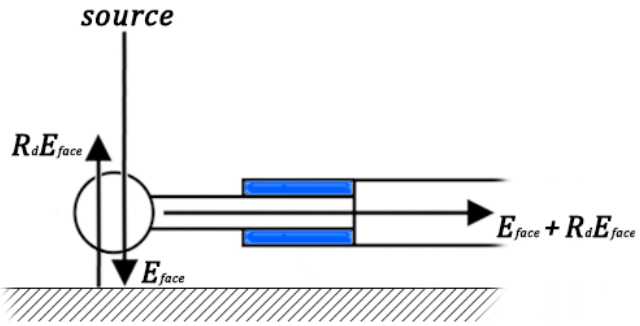

Figure 15 - Schematic visualization of the link between fluence rate and the irradiance on a surface. A light source shines light on a surface, this is described with irradiance E_{face}. Part of this irradiance reflects on the surface with a factor of R_d. Both the incoming light E_{face} and the reflected light R_dE_{face} is measured by the measuring probe, which together is the fluence rate.

The calculations of all these reflections were vectorized to improve calculation speed. Vectorization of the shadow determination was possible but limited the amount of faces that could be used for calculation. Vectorization needed a huge amount of memory. Therefore, the shadow determination was performed loop wise, which costs more time but enables to simulate light distributions in more detailed cavities.

3.2. Empiric approach

Next to the analytic approach an empiric approach was made that aimed to create a light distribution model that would be simple in calculations. This empiric model was created based on light fluence rate measurements performed in 3D printed tissue optical phantoms of patient specific sinonasal cavities (3DPPs) after maxillary surgery. The aim was to investigate the buildup β in fluence rate at the surface as a result of tissue reflection and diffuse remittance. The link (build-up function) between β and the distance between the surface and the light source was determined. This link between buildup and distance could then be implemented in the empiric light distribution model. Also, a link between β and geometrical properties of the cavity which can be derived from a CT scan i.e. cavity volume and cavity wall surface area was assessed. This assessment will help to explore clinical applicability possibilities of the empiric model.

3.2.1. Phantom creation

Three 3DPPs were made, three beige phantoms from 3 different patients (Figure 16). These phantoms were first digitally designed based on the patient specific CT scan. With the use of the medical image viewer and processing software kit '3D slicer', a threshold was applied on the CT scan to distinguish air from tissue. A STL-file was then exported which contained a 3D model of the patient's sinonasal cavity. This model was made ready for 3D printing by removing disconnected parts with a 3D modelling program 'Blender', followed by smoothing the model. A last check whether the model was ready for 3D printing was done with 'Meshmixer', which had the ability to check for defects that would cause problems during printing. The result was a digital model in STL-format that was ready for 3D printing.

Figure 16 - Frontal view of 3DPPs. Three phantoms were created with beige color.

The models were printed in Acrylonitrile Butadiene Styrene (ABS) for which μ_a and μ_s seemed to be most comparable with human tissue for light with a wavelength of 652 nanometer as confirmed by diffuse reflectance measurements performed by T. van Doeveren and R. van Veen.[34]

After printing the phantoms, holes were drilled externally into the cavity, entering the cavity on various locations of interest. These holes will facilitate a passage for optical measuring probes (outer diameter 1mm) into the cavity. In Figure 17 a photo of one of the phantoms to shows the interior of the cavity together with the locations of the drilled holes.

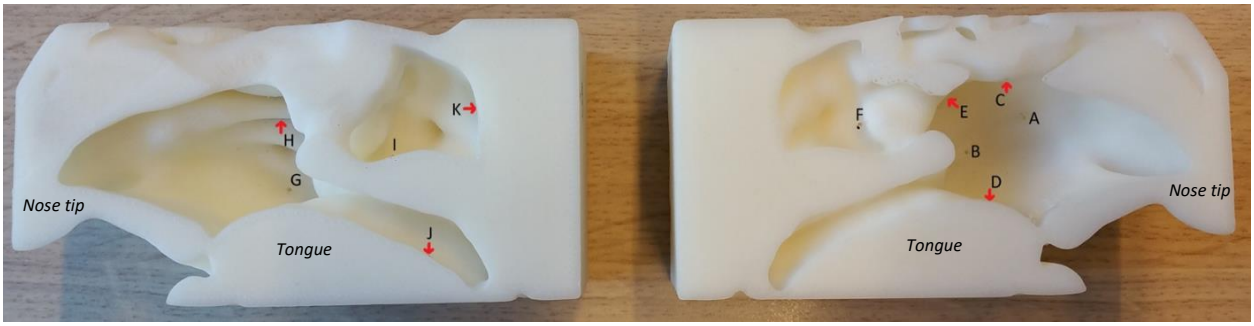

Figure 17 - 3DPP of sinonasal cavity, showing the interior of the phantom. The phantom is printed in halves to ensure proper measurement probe placement. The probe positions are indicated with letters

3.2.2. Measurements

A two-Watt diode laser (Ceralas PDT, Biolitec, Bonn, Germany) emitting 652 nm light was used to perform the measurements within the phantoms. The diode laser was calibrated in air within an incorporated integrating cylinder for a maximum output of two Watt. Light was guided from the diode laser into the 3D printed cavities with the use of optical quarts fibers, emitting light diffusively with a spherical diffuser (Medlight SA, Ecublens, Switzerland) or emitting light in a spot with a micro-lens (Medlight SA, Ecublens, Switzerland) (Figure 4).

Fluence rates within the cavities were measured with light measuring probes (model IP85, Medlight S.A., Ecublens, Switzerland) which were designed to collect light isotropic at their distal ends and guide this light towards their proximal ends where they can be coupled to the optical dosimetry device (NI PXI-1045

18-slot Chassis, National Instruments, Center for Optical Diagnostics and Therapy, Erasmus MC, Rotterdam, The Netherlands). The light measuring probes had a spherical tip at the distal end with a diameter of 0.85 mm and a core diameter of 400μm (Figure 18). Calibration of the probes was performed in air with the use of an integrating sphere and calibrated LEDs of which provided a known diffuse calibration field within the sphere.

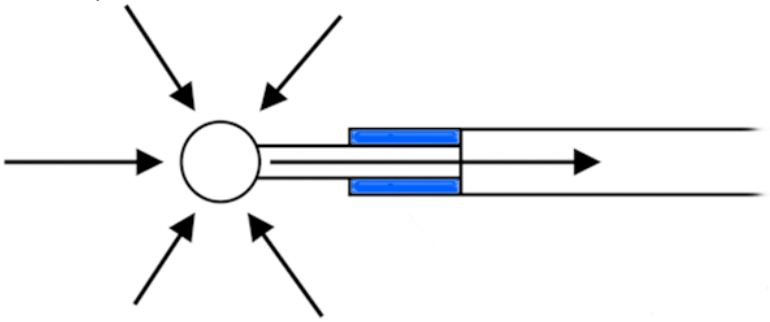

Figure 18 - Schematic visualization of the isotropic probe (model IP85, Medlight S.A., Ecublens, Switzerland). Arrows indicate light entering the probe, being transported via the fiber-based catheter towards the proximal end. The CT-marker is indicated in blue.

Eight calibrated measuring probes were guided into the 3D printed cavity via the pre-drilled holes in such a way that their distal ends were positioned just above the surface of the cavity wall (Figure 19). These distal ends were then able to measure fluence rates at locations of interest within the cavity. The probes were fixated with double-sided tape to secure proper position of their measuring ends within the cavity.

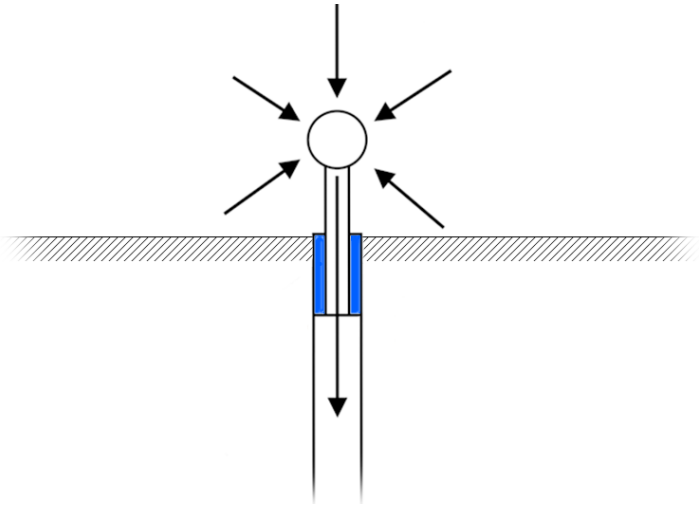

Figure 19 - Schematic representation of a measuring probe positioned through a drilled hole in the cavity, such that the distal end was just positioned above the surface of the cavity wall. The CT marker mounted in the fiber is highlighted in blue. The arrows indicate the direction of light.

Then the halves of the phantom were put together and fixated on the OR bench followed by placement of the light source i.e. spherical diffusor or micro-lens. The light source was kept in place after manual positioning with a surgical fixation arm (3840.67 Fisso, Zurich, Switzerland) to exclude fluence rate changes due to hand-held positioning. To prevent photons from outside entering the phantom and interfering with the measurement, the phantom was covered with wet green drapes (Figure 20).

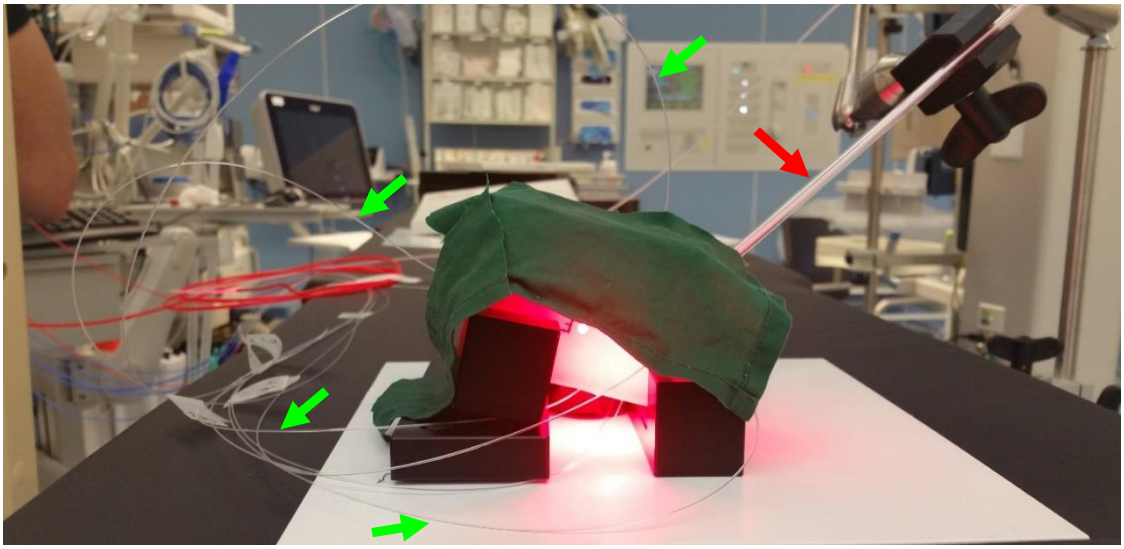

Figure 20 - Illuminated phantom during dosimetry measurement. The light source was guided into the phantom with a plastic tube (red arrow). The optical quarts fibers (green arrows) run from the measuring probes run from the optical dosimetry device into the phantom.

After preparing the setup of the measurement a CT scan was made of the setup with a cone beam CT (Xpert, Allura FD20, Philips) to capture the spatial information of the phantom, isotropic probes and light source. The positioning of the light source and measuring probes were checked and if necessary, changed. Once the light source and probes were positioned correct the measurement could start.

Four series of measurements were performed per phantom in which the fluence rate was assessed with eight measuring probes simultaneously at different locations. Two of them were carried out with a spherical diffusor and two with a micro-lens. Two positions were adopted for each light source i.e. anterior and posterior which differ approximately one centimeter. The output power of the spherical diffusor was set at 0.5 W and 0.31 W for the micro- lens.

The optical dosimetry devise measures fluence rate per timestep per measuring probe. An interval of 5 seconds near the end of each measurement period was used for analysis because the laser reached a constant output power after 10 seconds due to heating of the laser.

The CT scan made with the cone beam CT was used to measure the distances between probes and light sources. The distances between the light sources and the measuring probes was measured within these scans with the use of a measuring tool made in MATLAB®. A short accuracy test was performed to test the inter observer variability for this measuring tool. Three observers located all the light source and probe positions five times each. Al these chosen points were then put together and a rms of +/- 0.5 mm was measured. Together with the fact that the markers of the probes and light sources were not at the exact location a rms of +/- 1.5 mm is assumed. This indicated that for the measured distances had a rms of approximately $\sqrt{2} \cdot 1.5\ mm = 2.1\ mm \approx 2\ mm$.

3.2.3.Empiric model

An empiric light distribution model was created based on the measurements and the theory of the fluence rate build-up factor. In each patient-specific cavity, measuring probes were placed at eight different positions, all of which had their own distance to the light source. β could also be determined for each measuring probe. These β's could be linked to their distances with a build-up function. This cavity specific

build-up function $\beta(r)$ was used to predict the fluence rate in case of a spherical diffusor at the surface of the cavity wall with the following equation:

$$\varphi_{total} = \frac{P_{out}}{4\pi r^2}\beta_{diffusor}(r) \quad (22)$$

where P_{out} is the output power of the spherical diffusor, r is the distance between the light source and cavity wall and $\beta_{diffusor}(r)$ is the cavity specific build-up function for a spherical diffusor.

And in case of a micro-lens the fluence rate can be predicted with:

$$\varphi_{total} = \frac{P_{out}}{\pi(\tan(17{,}35°)\, r)^2}\beta_{lens}(r) \quad (23)$$

were $\beta_{lens}(r)$ is the cavity specific build-up function for a micro-lens and $tan\,(17.35°)$ factor in the denominator describes the fixed angle of the micro-lens i.e. numerical aperture, that is used.

For simulation purposes $\beta(r)$ must be determined. In clinical practice it is not feasible to have a lot of measuring probes positioned the in the sinonasal cavity as was used in the 3DPP studies described above. Determining $\beta(r)$ with less measuring probes is desired to make it clinically applicable i.e. one, two or three measuring probes. However, determining $\beta(r)$ with less measuring probes will create fluctuations in $\beta(r)$ and is dependent on which measuring probes were used. Therefore, it was examined what the standard deviation will be, if a single probe (n=1) was used to determine $\beta(r)$. This is done by calculating $\beta(r)$ multiple times, each time with a single probe. Then the standard deviation of all these $\beta(r)$'s was calculated. The standard deviation was also calculated if $\beta(r)$ was determined with a combination of two measuring probes (n=2) and a combination of three measuring probes (n=3).

The relation between $\beta(r)$ and the volume of the phantom's cavity together with the relation between $\beta(r)$ and the surface area of the cavity wall was assessed.

3.3. Verification

The verification of both models consisted of simulations of the measured fluence rates in the phantom measurements described earlier. Only the measurements including the spherical diffusor were simulated as preliminary simulations of the micro-lens showed that simulations for the micro-lens were not yet possible due to the higher complexity of a micro-lens.

3.3.1.Analytic model

The input of the analytic light distribution model is a CT scan of the cavity, light source location, light source power and the diffuse reflectance coefficient of the faces R_d. An assumption of the value of R_d was made, followed by manually fitting R_d by minimizing the root mean square (rms) between measured and simulated fluence rates.

The output of the analytic model is a surface for which each face the fluence rate was simulated. To compare this simulation with the measured values in the phantoms the values were extracted from the simulated surface at the positions of the measuring probes. The CT-scans were used to locate the positions of the measuring probes on the simulated surface.

A sanity check was performed on the analytic simulations, to check the total amount of light present within the cavity and whether this was constant. This quantity must logically remain constant and should not increase of decrease per reflection. This sanity check was performed at two moments in the simulation. The first moment was when the direct incident light fall was simulated on the wall of the cavity. The second moment was when all reflections where simulated. The used equations are equations (24) and (25).

$$Percentage\ of\ direct\ incident\ light\ fall = \frac{\sum_{k=1}^{m} E_{direct,k} A_k}{P_{out}} 100\% \quad (24)$$

where P_{out} is the output power of the light source, A_k the surface area of the face, E_i the direct incident irradiance received by the face, m the total amount of faces that make up the cavity surface.

$$Percentage\ after\ reflections = \frac{\sum_{k=1}^{m} E_{face,total,k} A_k}{P_{out}} 100\% \quad (25)$$

where P_{out} is the output power of the light source, A_k the surface area of the face, $E_{face,total}$ the total irradiance on a face after all simulated reflections, m the total amount of faces that make up the cavity surface.

3.3.2. Empiric model

The input of the empiric light distribution model is the CT scan of the cavity, light source location, light source power and the cavity specific $\beta(r)$. This patient specific $\beta(r)$ was made based on all measurement points within the cavity.

The output of the empiric model is a surface for which each face the total fluence rate was simulated. To compare this simulation with the measured values in the phantoms the values were extracted from the simulated surface at the positions of the measuring probes.

3.4. Validation

The validation of both models consisted of simulations of the measured fluence rates of the measurements in the TP. Just like in the verification section only the measurements including the spherical diffusor were simulated.

3.4.1. Phantom creation

A TP was made which consists of a 3D printed shell, cloaked inside with porcine meat. The 3D Voronoi mesh was created in 'Meshmixer'. First a simplified slightly oversized sinonasal cavity shape was made. Then this shape was hollowed and meshed so that it forms a shell-like structure as can be seen in Figure 21. Meshing the shell makes it easier to attach the meat to the shell and even reduces costs and time.

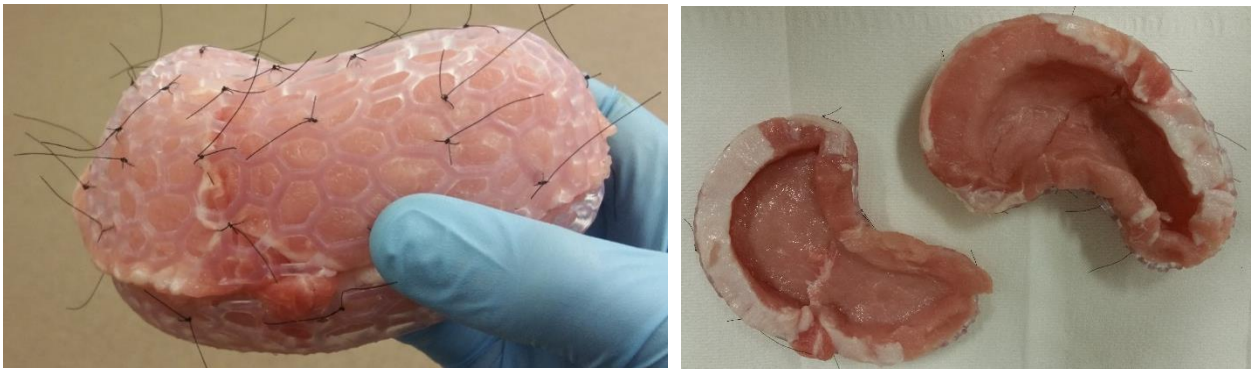

Figure 21 - Tissue phantom which was supported by a 3D printed shell. Left picture visualizes the assembled tissue phantom and right picture visualizes the two separate halves that make up the phantom, giving a view of the interior of the phantom. The porcine meat was sutured into the shell with ethilon 4.0 sutures.

3.4.2. Measurements

The fluence rate measurements in the TP were conducted in a similar way as the 3DPPs.

Eight calibrated measuring probes were guided into the tissue cavity via infusion needles in such a way that their distal ends just positioned above the surface of the cavity wall as visualized in Figure 19. These distal ends were then able to measure the fluence rate at locations of interest within the cavity. The probes were fixated with the use of double-sided tape and blocks to secure proper position of their measuring ends within the cavity (Figure 22).

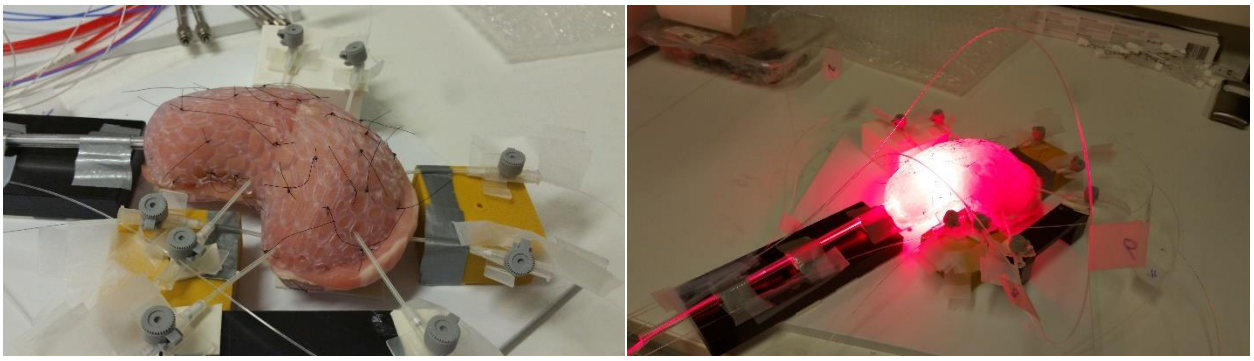

Figure 22 - Tissue phantom in which the light source and measuring probes are positioned. The measuring probes are guided into the tissue phantom with infusion needles which are fixated on Perspex blocks. Left is a visualization of the setup with laser switched off and right is a visualization of the setup with the laser switched on.

Then the two phantom halves were put together and fixated on a platform followed by placement of the light source i.e. spherical diffusor. The light source was kept in place after manual positioning by fixating it on a Perspex block to exclude fluence rate changes due to hand-held positioning.

After the measurements CT scans were made of the setup with a CT scanner (Somatom, Sensation Open, Siemens) to capture the spatial information of the phantom to calculate the distances between isotropic probes and light source.

Two measurements were performed in the phantom in which the fluence rate was assessed with eight measuring probes simultaneously at different locations. The measurement was carried out with a spherical diffusor and micro-lens, for which two positions were adopted. The second position was adopted

by manually retracting the fiber approximately two centimeters. The output power of the spherical diffusor was set at 1.5 W and the output power of the micro-lens was set at 0.35 W.

The analysis of this measurement was performed the same way as for the measurement in the 3DPPs.

3.4.3.Analytic model

The same methods were used for the validation of the analytic model as were described for the verification of the analytic model except that the simulation was made within the TP instead of a 3DPP.

3.4.4.Empiric model

The same methods were used for the validation of the empiric model as were described for the verification of the empiric model except that the simulation was made within the TP instead of a 3DPP.

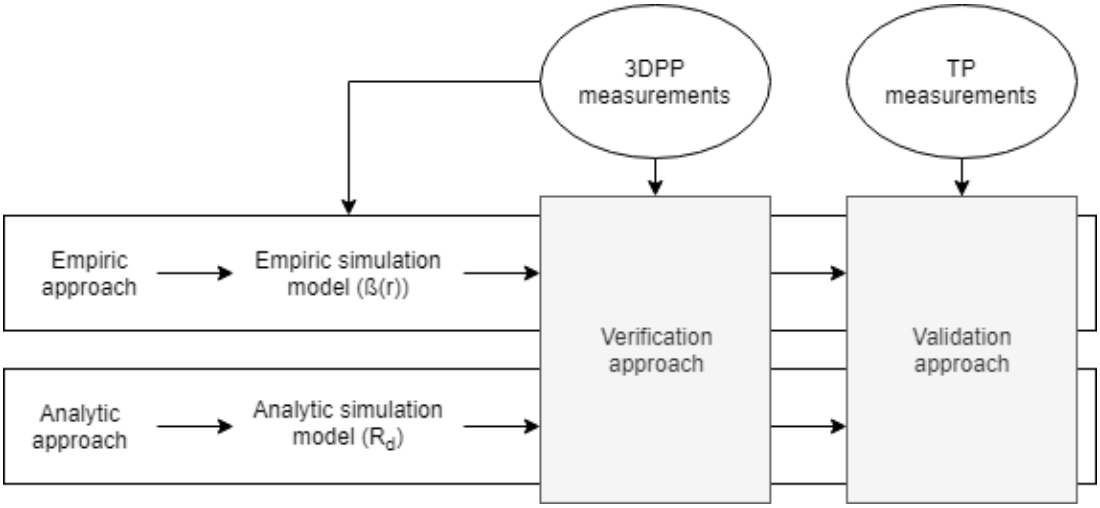

Figure 23 - Overview of all the components described in the methods section. Two approaches were taken to develop a light distribution model i.e. 'empiric approach' and 'analytic approach'. These approaches generated both a simulation model, respectively empiric simulation model and the analytic model which were dependent of the build-up function $\beta(r)$ and the diffuse reflectance coefficient R_d. The 3DPP measurements were needed for the creation of the empiric simulation model and the verification of both models. The TP was used to validate both simulation models.

4. Results

4.1. Empiric approach

4.1.1. Phantom measurements

Measured dosimetry values for all four series of measurements within the 3DPP are put together in Table 1.

Phantom type	Light delivery	Position	Laser output (mW)	Probe 1 (mW/cm²)	Probe 2 (mW/cm²)	Probe 3 (mW/cm²)	Probe 4 (mW/cm²)	Probe 5 (mW/cm²)	Probe 6 (mW/cm²)	Probe 7 (mW/cm²)	Probe 8 (mW/cm²)
Patient 1	Lens	A	310	29.9	42.7	224.9	59.0	42.9	7.5	31.3	29.6
Patient 1	Lens	P	310	26.3	46.2	416.8	64.6	38.9	6.8	28.2	27.2
Patient 1	Spherical	A	500	85.5	30.1	50.6	42.4	183.4	21.7	75.8	70.4
Patient 1	Spherical	P	500	80.0	38.1	71.4	56.8	115.8	18.6	77.7	68.4
Patient 2	Lens	A	310	102.0	94.5	75.2	99.5	93.0	241.6	167.2	196.2
Patient 2	Lens	P	310	111.2	175.1	80.4	172.4	92.7	108.0	311.2	374.1
Patient 2	Spherical	A	500	209.6	118.8	156.2	137.7	223.4	242.6	150.8	131.8
Patient 2	Spherical	P	500	243.1	163.9	183.1	187.7	239.1	360.7	215.1	185.7
Patient 3	Lens	A	310	36.5	43.4	30.8	29.4	603.0	18.2	18.4	7.8
Patient 3	Lens	P	310	43.6	48.8	41.1	30.3	150.6	20.5	21.6	9.4
Patient 3	Spherical	A	500	97.6	121.9	88.4	95.3	73.2	54.7	60.3	15.6
Patient 3	Spherical	P	500	100.8	132.4	97.6	90.8	92.5	55.0	61.1	16.5

Table 1 - Dosimetry measurements in 3DPPs. It is assumed that the measurements have an error of 5-10%. [17,35,36] *In column 'Position', 'A' stands for an anterior position and 'B' for a posterior position.*

What stands out in this table is that the fluence rates in patient 2 are substantially higher for the spherical diffuser than the fluence rates in the other two patients illuminated with a spherical diffuser while the laser output is the same. Closer inspection of Table 1 shows high fluence rates for probes which are directly illuminated with a micro-lens, whereas the other measuring probes receive much lower fluence rates. This difference between these measuring probes is higher in case of a micro-lens then in case of a spherical diffuser.

An overview of the distances between the light source and the measurement probes is made in Table 2.

Phantom type	Light delivery	Position	Probe 1 (mW/cm²)	Probe 2 (mW/cm²)	Probe 3 (mW/cm²)	Probe 4 (mW/cm²)	Probe 5 (mW/cm²)	Probe 6 (mW/cm²)	Probe 7 (mW/cm²)	Probe 8 (mW/cm²)
Patient 1	Lens	A	3.3	1.4	0.8	1.9	3.2	6.1	3.5	4.3
Patient 1	Lens	P	3.5	1.5	0.8	1.9	3.3	6.2	3.4	4.2
Patient 1	Spherical	A	1.9	3.6	3.9	3.9	0.8	3.9	3.0	3.1
Patient 1	Spherical	P	2.0	2.6	2.6	2.9	1.3	4.5	3.2	3.3
Patient 2	Lens	A	2.2	1.2	2.6	1.0	2.5	1.1	1.1	0.4
Patient 2	Lens	P	2.3	1.2	2.7	1.2	2.4	1.9	1.1	0.3
Patient 2	Spherical	A	1.2	2.6	1.8	2.2	1.1	1.0	1.6	2.1
Patient 2	Spherical	P	1.3	2.1	1.8	1.7	1.0	0.6	1.0	1.4
Patient 3	Lens	A	1.6	1.4	2.2	2.2	2.1	4.9	3.5	5.5
Patient 3	Lens	P	2.0	1.6	2.1	2.5	1.6	5.2	3.8	4.1
Patient 3	Spherical	A	1.7	1.5	2.0	1.5	2.9	4.3	3.4	5.7
Patient 3	Spherical	P	1.9	1.5	1.9	1.8	2.2	4.7	3.5	5.3

Table 2 - Distance measurements with the use of cone beam CT scans. Distances between the light source and each measuring probe is depicted in centimeters. The rms of these measurements is estimated at approximately +/- 0.2 cm (see below). In column 'Position', 'A' stands for an anterior position and 'B' for a posterior position.

The build-up factors β are calculated for all three 3DPPs and visualized in Figure 24, a pattern in these factors can be seen when they are plotted against the distance between light source and measuring probe. Please note that these plots include only the measuring points that have received direct incident light.

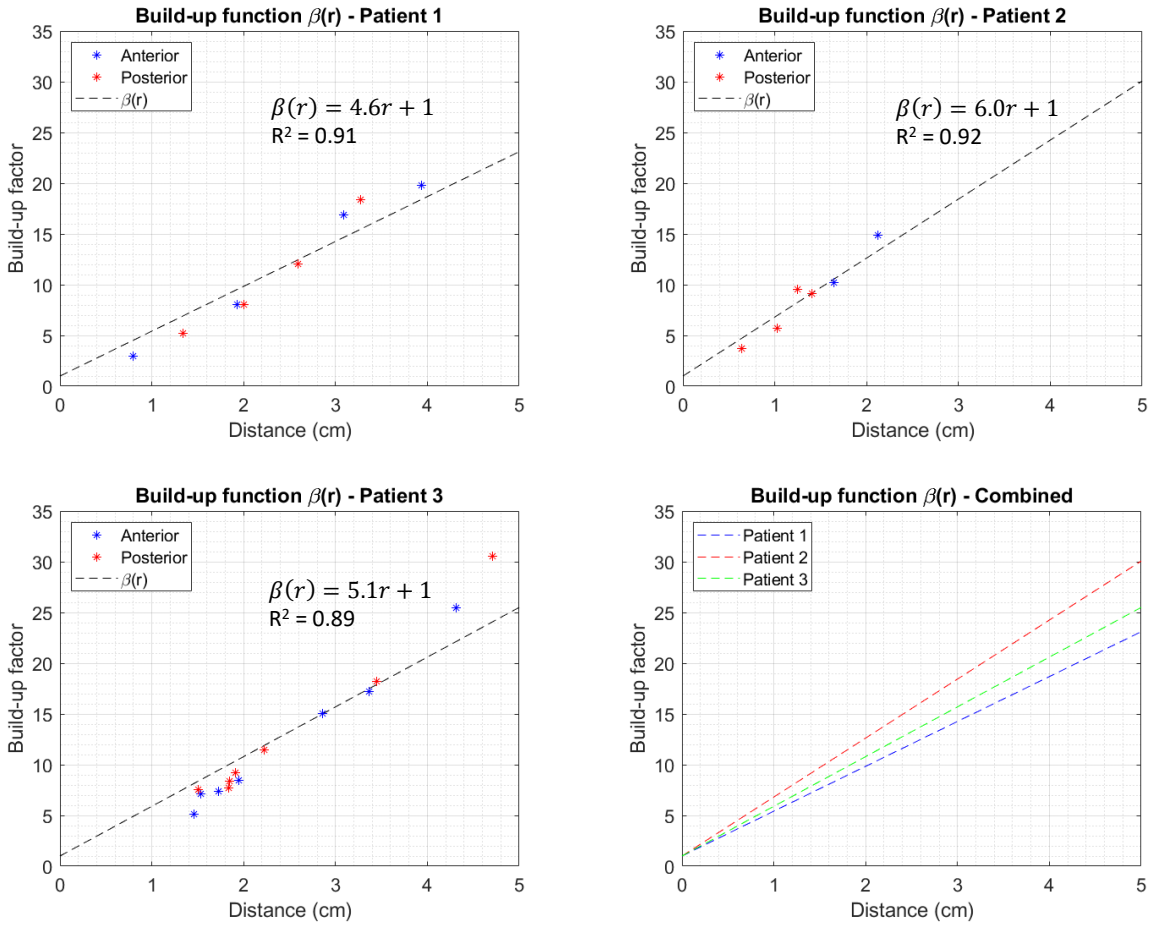

Figure 24 - 3DPP build-up function i.e. β(r). Depicts the distance dependency of the build-up factors in case of a spherical light diffusor. The visualized points represent all the measuring probes that received direct incident light from the light source. All other points were excluded because these did not receive direct incident light and therefore the build-up factor could not be calculated (equation (6)). The x-axis depicts the distance in centimeters between light source and measuring probe and the y-axis depicts the dimensionless build-up factor. A linear trendline i.e. 'build-up function' is calculated in the form of β(r)=ax + 1. How well $\beta(r)$ the β 's describes is expressed in a coefficient of determination R^2 for all three phantoms.

What is striking is that the data suggest that even with a changing light source position, all calculated build-up factors can be described with a linear function. These linear functions possessed a coefficient of determination (R^2) of around 0.9 is achieved in all 3DPPs. The linear function is fitted through the measurement points and point (0,1), as it is assumed that the build-up factor at zero distance between the light source and measuring probe is equal to one. Therefore, the linear function which describes the distance dependency of the build-up factors, is described in the following form:

$$\beta(r) = ar + 1 \tag{26}$$

where a is the slope of the linear function and r is the distance between the light source and measuring probe in centimeters.

The β's calculated for the measuring probes that did not receive initial light did not follow this trendline and were all lower than the trendline would have suggested.

The standard deviations in a of $\beta(r)$ caused by the reduction of the used number of measuring probes, are calculated and visualized in the figures below (Figure 25).

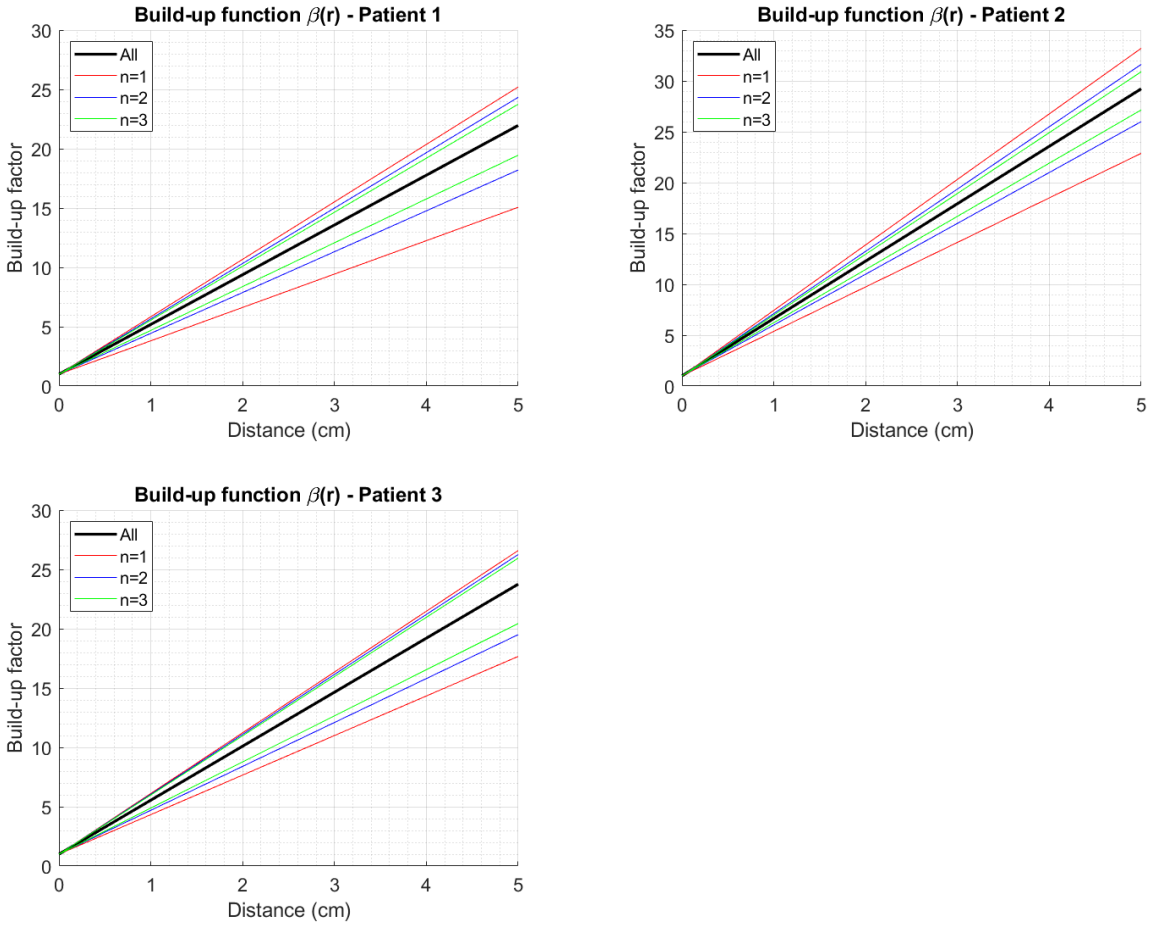

Figure 25 - Variances in the slope of $\beta(r)$ due to the number of measuring probes used to determine $\beta(r)$. 'All' is the build-up function determined with all measuring points, 'n' indicates the number of measuring probes used to determine the build-up function. These lines indicate the standard deviation per n used measuring probes. 'All' is 8, 6 and 14 for respectively patient 1,2 and 3.

The standard error caused by the reduction of the measuring probes is smaller the more measuring probes are used to create the $\beta(r)$. The variances are not always evenly distributed among the most ideal $\beta(r)$, indicating that the mean build-up function per 'n' is shifting as well. This mean is shifting towards the most-ideal $\beta(r)$ with increasing 'n'.

The link between a of $\beta(r)$ and the cavity volume and the link between a of $\beta(r)$ and the cavity wall surface area is visualized in Figure 26 and Figure 27.

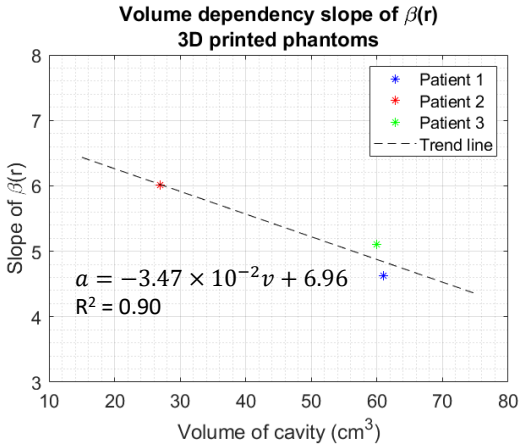

Figure 26 - Volume dependency of build-up slope. This plot visualizes the relationship in the measurements between the calculated build-up function coefficient and the volumes. The equation of the trendline is calculated and visualized as: $a = -3.47 \times 10^{-2} r + 6.96$, in which 'v' is the volume of the cavity in cm³ and 'a' is dimensionless.

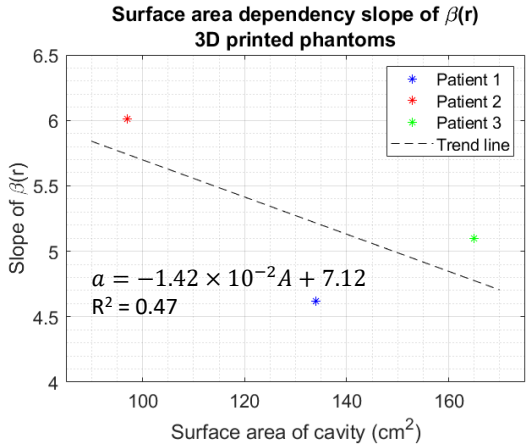

Figure 27 - Surface area dependency of build-up slope. This plot visualizes the relationship in the measurements between the calculated build-up function coefficient and the surface area of the cavity wall. The equation of the trendline is calculated and visualized as: $a = -1.42 \times 10^{-2} A + 7.12$, in which 'A' is the surface area of the cavity wall in cm² and 'a' is dimensionless.

A decreasing trend in the slope of the build-up function was examined with increasing cavity volume and a decreasing trend was examined with an increasing surface area of the cavity wall.

4.2. Verification

Each measurement in the 3DPPs is simulated with both light distribution models. The results of these simulations are explained below together with a comparison between the simulations.

4.2.1.Analytic model

The analytic model simulates the light distribution in approximately 15.9 seconds. For each face the fluence rate is calculated, so the output is a mesh of cavity faces with their own simulated fluence rate. An example is visualized in Figure 28.

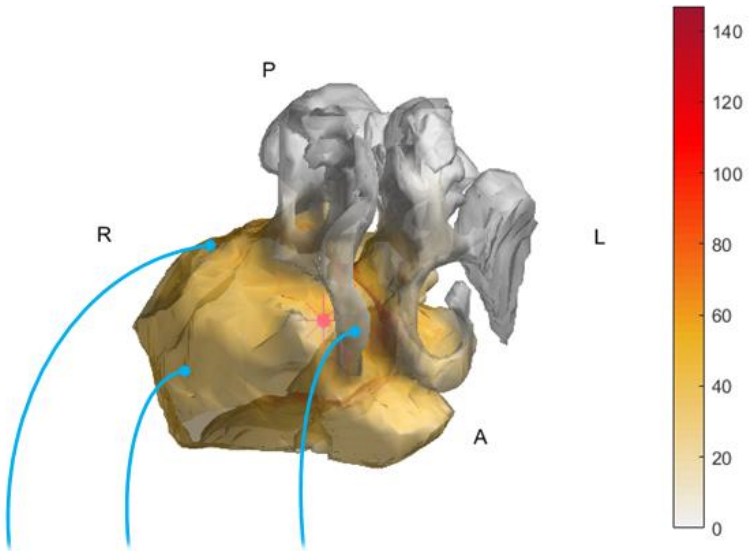

Figure 28 – 3D representation of the sinonasal cavity of patient 1. A frontal view is created which is slightly shifted to the right relative to the patient's head. The colormap shows the simulated fluence rate. The orientation of the cavity is marked with the letters A, P, L and R which stand for respectively anterior, posterior, left and right. The location of the spherical light source is indicated with a magenta star in the middle. The blue lines indicate some example spots where the measuring probes have been positioned and which fluence rates should be compared with the measurements.

The only unknown parameter of the analytic model is the diffuse reflectance coefficient R_d. The R_d of the ABS material of the 3DPPs was unknown, therefore it was fitted manually by minimizing the rms between measured and simulated values. A R_d of 0.81 was acquired. This roughly shows that 81% of the light quantity is sent back into the cavity per reflection. The amount of reflections that are then simulated is set to 22, since after 22 reflections the amount of light is below 1% of the light emitted by the light source ($P_{out}0.81^{22} = P_{out}0.0097$). In the appendix the effect of the number of reflections on the simulated fluence rates is in deeper detail elaborated. The simulated fluence rates are compared with the measured fluence rates together with the fitting graph of R_d in the graphs below (Figure 29).

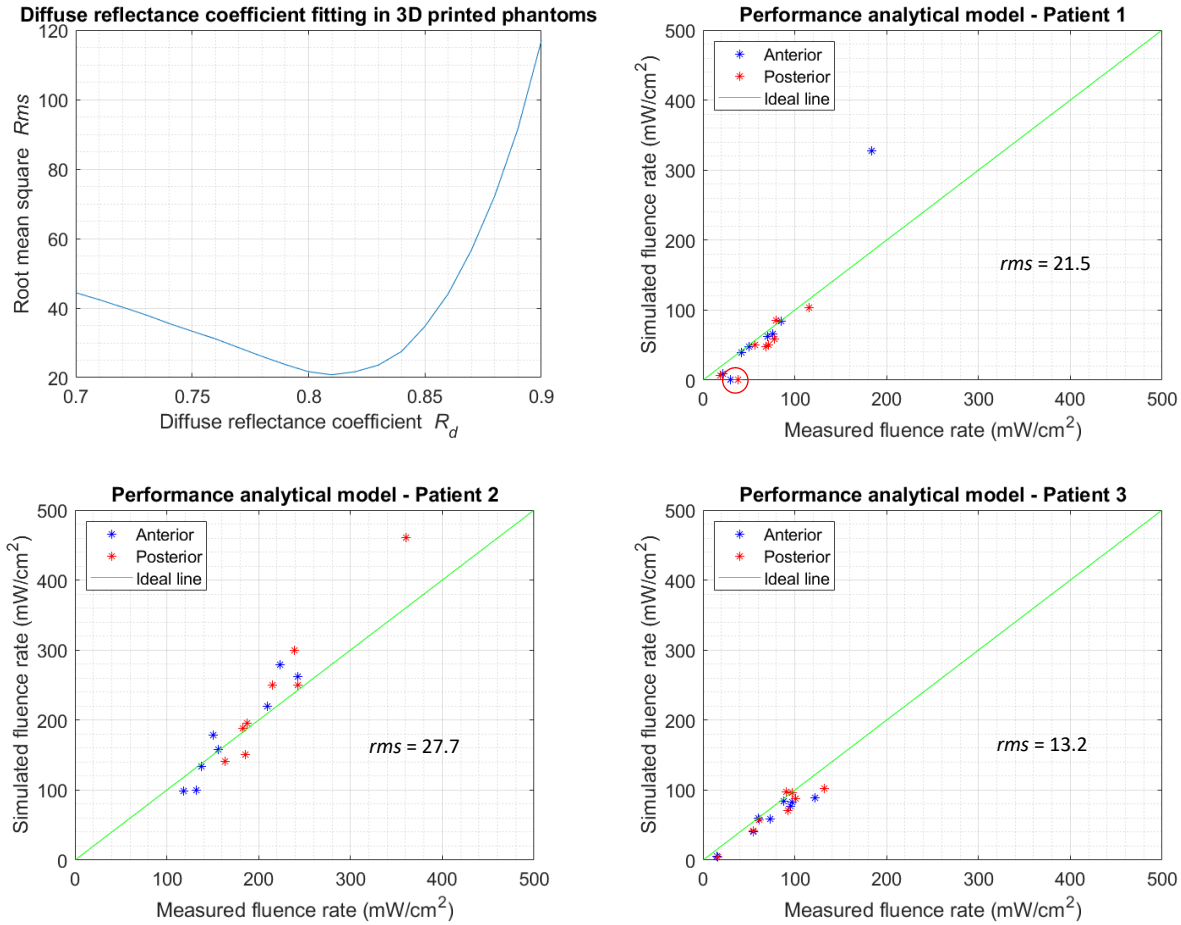

Figure 29 - The fitting and performance plots of the analytic simulations. Fitting of R_d was based on the mean rms of all measured positions in all three phantoms. R_d is changed with steps of 0.01 to find the lowest rms. A minimum rms value of 20.8 was found in the simulation with a R_d of 0.81. The simulated fluence rates, in case of a spherical diffusor, in the 3DPPs are plotted against the measured fluence rates for each measuring probe position for two light source positions i.e. posterior and anterior. This simulation uses the fit R_d of 0.81 and simulates 22 reflections. The performance of each simulation is expressed in a rms value. The red encircled points represent a measuring point in a cavity that was not connected with the illuminated cavity, hence this is the same measuring probe because two measurements are performed per phantom altering the light source location i.e. anterior and posterior.

The simulated fluence rates follow the same trend as the measured fluence rates as can be seen in Figure 29. The mean rms of all three measurements is 20.8 which is achieved with an R_d of 0.81. What is striking is that the plots of patients 1 and 2 both have an outlier at a point where a high fluence rate is measured. It is also important to see that there are two points that have a simulated fluence rate of zero while the measured fluence rate is around 30-40 mW/cm^2. These two points are encircled with a red line.

The results of the sanity check are visualized in Table 3 for the anterior and posterior spherical diffusor locations.

Phantom type	Position	Direct incident light fall	After 22 reflections
Patient 1	A	102.7%	125.5%
Patient 1	P	98.8%	114.7%
Patient 2	A	101.1%	131.4%
Patient 2	P	101.2%	132.2%
Patient 3	A	100.3%	128.7%
Patient 3	P	101.1%	126.1%

Table 3 - Sanity check of analytic simulation of 3DPPs. Percentages represent the total amount of simulated energy on the wall of the cavity in relation to the input energy. Column 'Initial' represents the percentages of the simulated direct incident light. Column 'Reflections' represents the percentages of the total simulated light within the cavity after 21 reflections. In column 'Position', 'A' stands for an anterior position and 'P' for a posterior position.

This table shows that the total amount of light present within the cavity exceeds the total amount of light emitted by the light source. After 22 reflection this total amount becomes larger.

4.2.2. Empiric model

The empiric simulation model simulates the light distribution in approximately 8.0×10^{-5} seconds. The simulated fluence rates are compared with the measured fluence rates in the graphs below (Figure 30). These graphs show the simulated fluence rates, using the predetermined $\beta(r)$ in the phantom measurements described above. This simulation is the best possible simulation that can be achieved with these measurements because it uses the $\beta(r)$ which is determined with all the measuring probes that received direct incident light in the measurement.

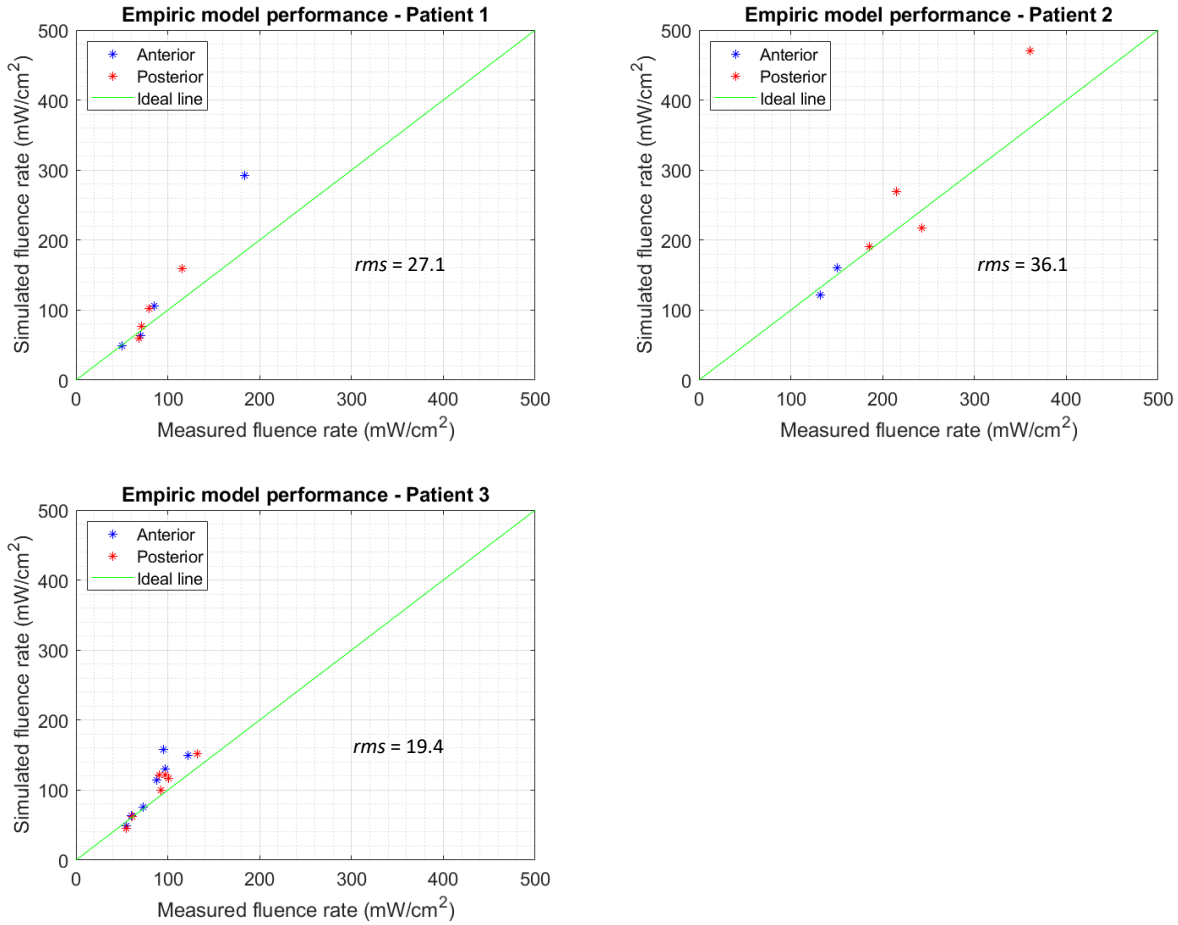

Figure 30 - The simulated fluence rates with the empiric model for the 3DPPs are plotted against the measured values. The simulation is made with the build-up function created with the use of all measurement positions that received direct incident light from the light source. This simulation is thus the best simulation that can be achieved with the empiric simulation for these measurements. The performance of each simulation is expressed in a rms value.

The simulated fluence rates follow the same trend as the measured fluence rates as can be seen Figure 30. Only the fluence rates of the measuring probes that received direct initial light could be simulated with the empiric light distribution model.

4.3. Validation

First a light dosimetry measurement is performed in the TP which is constructed from porcine tissue in order to mimic the sinonasal cavity in a clinical setting. Then these measurements were simulated with both simulation models.

4.3.1. Tissue phantom measurements

Measured dosimetry values in the TP are depicted below in Table 4. Four measurements were performed in this TP which consisted of two light sources which both have adopted two positions i.e. a posterior and an anterior.

Light delivery	Position	Laser output (mW)	Probe 1 (mW/cm²)	Probe 2 (mW/cm²)	Probe 3 (mW/cm²)	Probe 4 (mW/cm²)	Probe 5 (mW/cm²)	Probe 6 (mW/cm²)	Probe 7 (mW/cm²)	Probe 8 (mW/cm²)
Lens	A	350	6.7	48.9	85.2	10.1	8.8	4.8	6.9	12.4
Lens	P	350	5.1	18.2	53.8	10.1	8.6	5.2	7.0	9.9
Spherical	A	1500	129.7	35.3	28.1	20.3	12.7	4.7	7.5	107.2
Spherical	P	1500	96.8	11.4	73.3	45.9	45.8	15.8	29.7	130.5

Table 4 - Dosimetry measurements of the TP. The measurements were performed in a fixed situation, resulting in a neglectable standard error for the mean measured values. In column 'Position', 'A' stands for an anterior position and 'P' for a posterior position.

What stands out in this table is that all measuring probes measured a significant change in fluence rate in case the spherical diffusor was moved. While movement of the micro-lens did not have such profound changes in measured fluence rates. Only probes 2, 3 and 8 showed some changes in measured fluence rate.

An overview of the distances between the light sources and the measuring probes is made in Table 5.

Light delivery	Position	Probe 1 (cm)	Probe 2 (cm)	Probe 3 (cm)	Probe 4 (cm)	Probe 5 (cm)	Probe 6 (cm)	Probe 7 (cm)	Probe 8 (cm)
Lens	A	1.8	4.9	6.5	7.4	6.9	6.1	6.3	2.1
Lens	P	1.2	2.5	4.0	5.7	5.4	5.7	5.4	1.7
Spherical	A	1.7	4.7	6.3	7.2	6.6	5.9	6.1	1.9
Spherical	P	2.1	1.8	3.2	5.0	4.9	5.3	4.9	1.9

Table 5 - Distance measurement of the TP. In column 'Position', 'A' stands for an anterior position and 'P' for a posterior position.

The corresponding β's of the tissue measurement, in case of a spherical diffusor, are calculated and visualized in Figure 31.

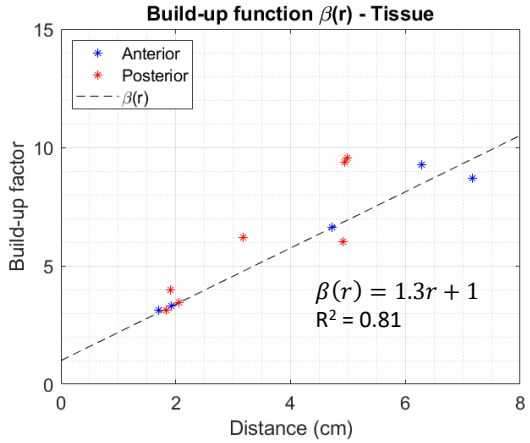

Figure 31 - The build-up function determined in the tissue phantom. Depicts the distance dependency of the build-up factor in case of a spherical light diffusor. The visualized points represent all the points that received direct incident light from the light source, all other points are excluded. How well $\beta(r)$ the β's describes is expressed in a coefficient of determination R^2 of 0.81.

The same linear function i.e. $\beta(r)$ is fitted through the calculated β's and point (0.1), just as is done and explained for the 3DPPs. A coefficient of determination (R^2) of around 0.8 is achieved in case of the TP. What stands out is that the slope of $\beta(r)$ is significantly lower than the slopes of $\beta(r)$ determined for the 3DPPs.

In Figure 32 the $\beta(r)$ determined with the β's from all measuring points that received direct incident light is visualized together with the standard deviation caused by reducing the number of measurement probes used to determine $\beta(r)$.

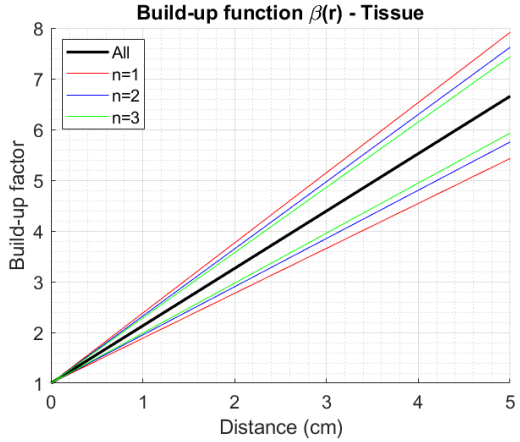

Figure 32 - Variances in the slope of $\beta(r)$ due to the number of measuring probes used to determine $\beta(r)$. 'All' is the build-up function made with all measuring points, 'n' indicates the amount of measuring probes used to determine the build-up function. These lines indicate the standard deviation per n used measuring probes. 'All' is in this case 12 measuring points.

The standard error caused by the reduction of the measuring probes is smaller the more measuring probes are used to create the $\beta(r)$, just as was seen for the 3DPPs.

4.3.2. Analytic model

The analytic model simulates the light distribution for the TP in approximately 7.9 seconds.
The R_d of the tissue was unknown, therefore it was fitted manually by minimizing the rms between measured and simulated values. A R_d of 0.62 was acquired which is visualized in Figure 33. This roughly shows that 62% of the light quantity is sent back into the cavity per reflection. The amount of reflections that were then simulated was set to 10, since after 10 reflections the amount of light is below 1% of the light emitted by the light source ($P_{out}0.62^{10} = P_{out}0.0084$). The simulated fluence rates are compared with the measured fluence rates in the graph below (Figure 34).

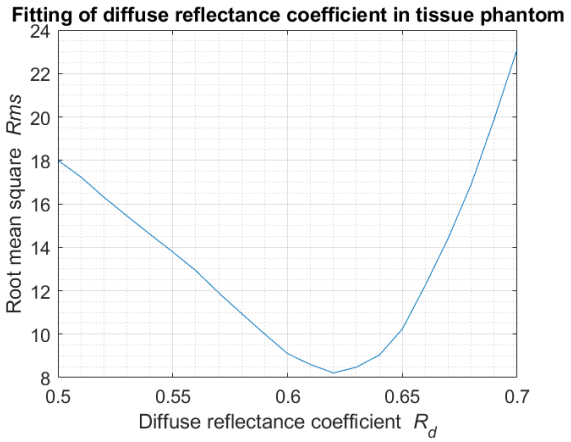

Figure 33 - Fitting of R_d based on the rms of all measured positions. R_d is changed with steps of 0.01 to find the lowest rms. A minimum rms value of 8.2 was found in the simulation with a R_d of 0.62.

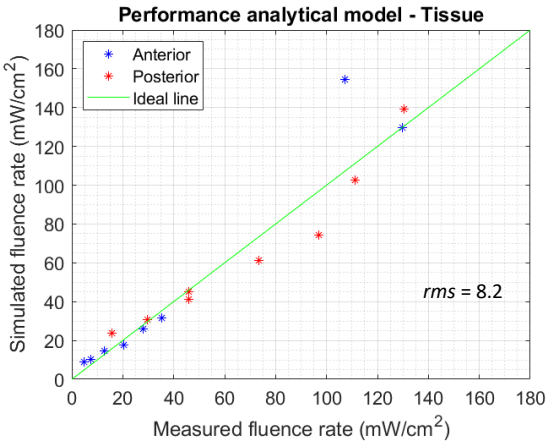

Figure 34 - The simulated fluence rates in case of a spherical diffusor in the TP are plotted against the measured fluence rates for all measuring probes for two light source positions i.e. posterior and anterior. This simulation uses a R_d of 0.62 and simulates 10 reflections. The performance of each simulation is expressed in a rms value.

The simulated fluence rates correspond well to the measured fluence rates as can be seen in Figure 34. The mean rms of this simulation is 8.2 which is achieved with an R_d of 0.62 (Figure 33).

The same sanity check as for the 3DPPs is performed for the TP. This time the total amount of light present after 10 reflections is examined. The results are depicted in Table 6.

Position	Direct incident light fall	After 10 reflections
A	102.1%	117.2%
P	99.3%	109.7%

Table 6 - Sanity check of analytic simulation of the TP measurement. Percentages represent the total amount of simulated energy on the wall of the cavity in relation to the input energy. Column 'Initial' represents the percentages of the simulated direct incident light. Column 'Reflections' represents the percentages of the total simulated light within the cavity after 10 reflections. In column 'Position', 'A' stands for an anterior position and 'B' for a posterior position.

This table shows that the total amount of light present within the cavity does not increase or decrease much in comparison with the 3DPPs, which is desirable. After 10 reflections the total amount of light present in the cavity is more than at the moment of the direct incident light fall.

4.3.3. Empiric model

The empiric simulation model simulates the light distribution in approximately 8.0×10^{-5} seconds. The simulated fluence rates are compared with the measured fluence rates in the graph below (Figure 35). This simulation is the best possible simulation that can be achieved with these measurements, because it uses the $\beta(r)$ which is determined with all the measuring probes that received direct incident light in the measurement.

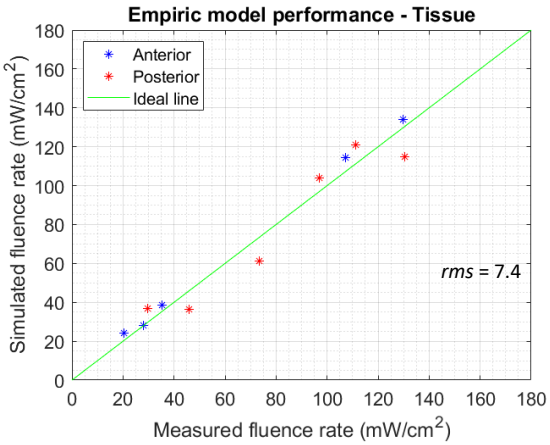

Figure 35 - The simulated fluence rates with the empiric model for the TP are plotted against the measured values. The simulation is made with the build-up function created with the use of all measurement positions that received direct incident light from the light source. This simulation is thus the best simulation that can be achieved with the empiric simulation for this measurement. The performance of the simulation is expressed in a rms value.

The graph above shows the simulated fluence rates for each measurement probe that received direct incident light during the measurement. No outliers are seen in this graph and in general, the simulated values correspond well to the measured values.

5. Discussion

5.1. Take home message

The long-term goal is to improve the efficacy of PDT by improving the planning that is done in advance. The first steps towards this goal are made by creating and testing an analytic and empiric light distribution model. It appears to be a challenging task to accurately simulate the light distribution measured in the experiments with a simple model, because there are a lot of factors that influence the light distribution. However, the light distribution models showed to be capable of simulating fluence rates within acceptable margins. The analytic light distribution model showed to be capable of simulating light distribution in the same trend and same magnitude among all measuring probes in each phantom. Thus it was even able to simulate the fluence rate at sites that did not receive direct initial light from the light source. The assumption of a Lambertian reflecting surface therefore seems a good assumption. The disadvantage of this light distribution model is that R_d had to be fitted. The empiric light distribution model was also capable of simulating the fluence rates in the same magnitude and had a short computation time. However this model could only be used to simulate the fluence rates of areas that were directly illuminated by the light source. Another disadvantage of this model is that $\beta(r)$ must be determined with less measuring probes than used in the measurements, which will result in greater variances in $\beta(r)$ and thus a less accurate prediction of the fluence rates.

5.2. Strengths and weaknesses

The two approaches i.e. analytic and empiric resulted in a broad approach in the pursuit of a clinically usable light distribution model. These approaches resulted in two light distribution models which were verified with phantom models and validated with a TP.

5.2.1.Measurements

CT scans were used to create a 1:1 scaled 3DPP of the patient's sinonasal cavity. Therefore, possessed these phantoms a genuine shaped and sized cavity. ABS white was used, which had a comparable scattering coefficient as mucosal tissue, but possessed a lower absorption coefficient. Also, the phantoms were 3D printed in one single material, which created a cavity with a wall whose optical properties were the same over the entire wall. The optical homogeneously cavity wall made it possible to assess the accuracy of the simulations in the most ideal conditions while the geometry of the cavity still influenced the light distribution. In practice the optical properties of the wall vary from place to place, which will probably cause a reduced accuracy.

The TP is a step towards a more realistic human sinonasal cavity. It was made of porcine meat and had dimensions comparable with human sinonasal cavities. Porcine meat ensured a more realistic optical properties of the cavity wall, still being reasonably homogeneous and suitable to construct a phantom with. Factors such as blood, mucus and crusts were not present in this phantom. Measurements in patients would have been the best way to validate the systems, however these measurements turned out to have their drawbacks regarding measurement options and accuracy. The narrow cavity allowed the use of only a few tools during the measurement. This resulted in that only one measuring probe could be positioned per measurement. Capturing the locations was also more inaccurate since no CT scan could be made and an EM-navigation system had to be used. EM-navigation is not per definition worse, but in our measurements we had only one tracking tool with which we could navigate the measuring probe and light source, resulting in uncertain placement and tracking. In the case of a TP, we were not limited in the amount of measuring probes that could be placed, also recording the probe positions was accurate since a CT scan could be made.

5.2.2.Analytic model

The analytic model calculates the light distribution in a cavity with basic radiometric equations and thereby uses the patient specific cavity to create a patient specific simulation. The advantage of this method is that the shadow effect can be predicted in a cavity. This is however a simplified raytracing method, thus creating minor errors in the predicted shadow effect in the cavity. Extensive, calculate intensive raytracing methods could be used, but they would only reduce the calculation speed.

The main drawback of the analytic model is that R_d was unknown. The R_d of the phantoms and TP was achieved by manually fitting the simulation data with the measured data to achieve an as low as possible rms, by in- or decreasing R_d in steps of 0.01 For future use the R_d should also be manually fitted or estimated. This forms a huge drawback of this model, because manually fitting will require a CT scan of the patient, the exact location of the light source and measuring probe within that cavity. This is clinically not achievable. A standard R_d could also be an option for the mucosa within specific body cavities. This will probably not differ much between people and the influence on the positioning would be minimal. The standard R_d also has room for a bit of variation when we look at the fitting curve Figure 33. Another option is to measure R_d fiber optically.[25,37,38]

5.2.3.Empiric model

The empiric model is built around the cavity specific $\beta(r)$, which grants simple calculations and high calculation speed. The distance dependent $\beta(r)$ makes the simulation more detailed than the static β used in literature.[25,29,33] It remains questionable whether this linear function is justified, but for the measurements we have done this function appears to be approximately linear, which also makes calculation easier. In contrast to the analytic model it lacks the ability to simulate light that does not receive initial light from the light source. These areas will only receive diffuse scattered light and will therefore be less illuminated in total than areas that have received direct incident light. Clinically, it remains questionable whether it is necessary to properly simulate these areas.

The empiric model is dependent on $\beta(r)$ which is estimated on multiple measuring points. In practice it is likely that less measuring probes can be used to measure fluence rates simultaneously and predict $\beta(r)$. So, in practice there will be a greater variation in $\beta(r)$ and therefore also in the simulated fluence rates.

5.3. Interpretation and mechanisms

5.3.1.Measurements

A R^2 of around 0.9 is achieved in all 3DPPs and 0.8 in case of the TP. A higher order equation could describe the β's better, however this will result in more complicated equations and caution must be applied to not overfit the measurement data. The lower value of R^2 suggest that the linear $\beta(r)$ describes the β's less within the TP. It could even be possible that $\beta(r)$ in the TP is dependent on the light source position, since the β's of anterior are generally lower than the β's of posterior which can be seen in Figure 31. It is important to bear in mind that only one TP measurement is done before conclusions can be drawn.

Since $\beta(r)$ is defined such that it starts in point (0.1), the only variable for this function is the slope. The variation in the slope due to the number of measuring points used is shown in Figure 25 for the 3DPPs and in Figure 32 for the TP. The standard deviation is relatively equal in both the 3DPPs and the TP, around +/- 20 mW for n=1. It is important to bear in mind that β is multiplied with the initial light fall to calculate the total amount of fluence rate present at a certain point (equations (22) and (23)). The amount of initial light decreases with increasing distance, resulting in lower absolute changes for greater distances.

One interesting finding is that the slope of $\beta(r)$ has a correlation with the volume of the cavity and the surface area the cavity's wall Figure 26 & Figure 27. This finding was also supported by Star et. al. who indicated the radius dependency of a spherical cavity with the measured fluence rates.[29] Caution should be applied when drawing conclusions, as there are probably more factors affecting the slope of the function e.g. erratic shape of the cavity.

5.3.2.Analytic model

Simulation of the 3DPPs with the analytic model showed promising results. With a R_d of 0.81 the model can approximate the measured fluence rates within acceptable margins. It can simulate the fluence rate at the surface by reflecting light from the cavity wall according to lamberts law of diffuse reflection to mimic the backscattering light from the tissue. However, it cannot simulate light through tissue. This is highlighted by the two measuring points encircled in Figure 29, which were located in a not connected sub-cavity and only obtained light that had traveled through the material of the phantom.

Another interesting finding is that high measured fluence rates in all 3DPPs are harder to simulate. This finding can be attributed to the fact that these high fluence rates are measured at positions that had small distances to the light source. For these position with small distances the relative error in distance measurement becomes larger and thus also the simulated fluence rate.

A sanity check is performed on the analytic simulations of the 3DPPs, which showed reliable results for the direct initial light fall i.e. the total irradiance on the entire simulated surface dived by the total surface area equals the total energy emitted by the source. However, when multiple reflections are simulated, the total amount of energy within the cavity grows. Ideally this should not grow and be constant at 100% of the light emitted by the light source. Each successive reflection is calculated the same way and probably includes minor errors which do increase the total amount of energy on the cavity wall. An explanation of these errors may be that the raytracing algorithm is too coarse. It determines for each face whether it is illuminated or not in steps of one-third. Thus, a face may be fully illuminated, for two thirds, one third or not illuminated at all. A slight overestimation can take place if a face should be illuminated for ½ of its surface but in the simulation, it is illuminated for ⅔ because the simulation cannot illuminate ½ of a face's surface. An underestimation can be made in the same way. Another explanation is the fact that the inverse square law incorporated in equation (16) is not applicable in case of relatively large surfaces. The original equation described by F. van der Heijden, states that A_1 should approximate relatively small values, however in the simulations these A_1's possessed significant values.[32] The mean surface area was 2.4 mm^2 with peaks of around 39 mm^2. This resulted in an overestimation of irradiance on a face. This phenomenon is explained and visualized in a simplified 2D example in Figure 36.

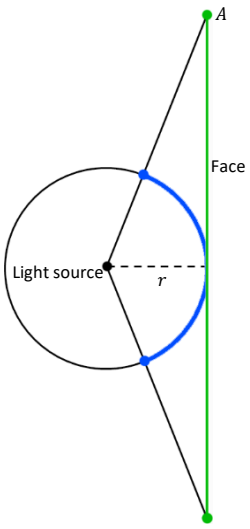

Figure 36 - Schematic explanation why the inverse square law equation overestimates the irradiance on a face in case of a relatively small r and large face surface area. In the middle a spherical light source is positioned which diffusively radiates energy. A face is drawn with a green line and a dotted line indicating the distance between the light source and face. This face receives light from the light source and the irradiance on the whole face is calculated with the inverse square law: $E = \frac{P_{out}}{4\pi r^2}$. This is a rough estimation for small r's, because as you look at the distance between point A and the light source then this distance is more than twice the length of r. This will result in a lower actual irradiance on that specific point on the face. If we do that for more points, we see that an overestimation occurs if we use the distance r to estimate the irradiance on the whole face.

In case of a relatively large face area with respect to the distance, the approximation of that surface with the inverse square law is an underestimation. The inverse law is used in the calculation of the irradiance. An underestimation of the surface area results in an overestimation of the irradiance (mW/cm^2). This results in higher simulated irradiances and thus higher simulated fluence rates. A possible improvement would be to generate a mesh that has faces with smaller surface areas. This will not solve the problem entirety because each face acts as a light source in the calculations of the reflections (Figure 13 & equation (16)).

In case of the TP a lower overestimation of total energy can be examined relative to the overestimation in the 3DPPs. This can be explained by the fact that the R_d in the TP is lower than the R_d in the 3DPPs due to higher absorption coefficient. Therefore, less reflections need to be simulated, thus less overestimation occurs.

5.3.3. Empiric model

Simulation with the use of the empiric model showed promising results. The simulated values lay within acceptable margins from the measured fluence rates and just like with the analytic model the fluence rate is hardest to simulate at measuring points with high fluence rates and small distances. The accuracy of the simulated fluence rates may be a bit too optimistic as these fluence rates are calculated with $\beta(r)$ which is derived from the same measurements. It must therefore be kept in mind that the simulation values in clinical practice may differ more from reality as fewer measuring points can be used to determine $\beta(r)$.

Both simulation models showed better absolute results when used to simulate the fluence rates measured within the TP, this is because the absorbance of tissue is higher. Resulting in lower measured fluence rates, which result in lower absolute differences between measured and simulated fluence rates. The relative difference in simulated and measured fluence rates is comparable with those in the 3DPPs.

5.4. Comparison Analytic versus Empiric

Comparing both models based on how well they can simulate the measured values, the rms scores provide insight into this. The average rms of the analytic model simulations for the 3DPPs was 20.8 (21.5, 27.7 and 13.2) and for the empiric model simulation 27.5 (27.1, 36.1 and 19.4). These average rms suggest a slight favor for the analytic model. For the TP measurement, the analytic model had a rms of 8.2 and the empiric model had a rms of 7.4 which indicates a slight favor for the empiric model. Looking at these rms of the simulations and their significance, it can be concluded that both models have comparable accuracy. A preliminary conclusion would be that the higher the absorption becomes, lesser amount of reflections will occur, resulting in more accurate predictions by both models.

It must be kept in mind that R_d is manually fitted to match the measurements best regarding the rms. In clinical practice the R_d must be estimated which will result in accuracy lost. The question remains how accurate R_d must be estimated and if a standard R_d for sinonasal cavities is possible to ensure that the simulation simulates fluence rates are within acceptable margins. Fiber optical measurements are also a viable option, the question remains how error sensitive these measurements are as these measurements can vary between different measurement spots on the cavity wall. Fitting R_d is assumed to be a non-viable option as a CT scan needs to be acquired before the procedure of the cavity in which the measuring probes and light source are positioned. This is unpractical.

A standard R_d could also be an option for the mucosa within specific body cavities. This will probably not differ much between people and the influence on the positioning would be minimal. The standard R_d also has room for a bit of variation when we look at the fitting curve Figure 33. Another option is to measure R_d fiber optically.[25,37,38]

It must also be kept in mind that $\beta(r)$ is determined with the fluence rates measured by all the measuring probes that received direct incident light from the light source. In clinical practice the amount of measuring probes would be limited, resulting in a less accurate $\beta(r)$ and thus less accurate simulations. This effect is expressed in Figure 25 and Figure 32. Keep in mind $\beta(r)$ is multiplied with the direct incident light fall, which reduces with increasing r, thus reducing the effect of the possible inaccuracy of $\beta(r)$. Regarding the applicability in clinical practice this model would be a viable option, because the measurement that must be done in advance does not inclu de a CT scan in which the light source and measuring probes must be located as the analytic pre-measurement does. What is needed for this simulation is a dosimetry measurement in which the distance between the light source and measuring probes are known. It is important to bear in mind that the simulation works if the light source is located near the light source location used in the measurement. It is unknown if the simulation is still valid if the light source is further away from the light source location in the measurement.

An overview of all the compared features of both models are summarized in Table 7 below.

Feature	Analytic model	Empiric model
Calculation speed (ABS – Tissue)	Slow (15.9 - 7.9 sec.)	Fast (8.0×10^{-5} - 8.0×10^{-5} sec.)
Rms (ABS – Tissue)	20.8 – 8.2	27.5 – 7.4
Variables	R_d	$\beta(r)$
Requirements to perform calculations.	3D position of light source and CT scan of cavity.	Distances between light source and point of interest.
Shadow determination	Able	Not able
Pitfalls	Simplistic raytracing algorithm and inverse square law usage for large face's in comparison to the distance between source and face.	Linear assumption of $\beta(r)$ through (0,1).
Clinical applicability	Harder to implement	Easier to implement

Table 7 - Overview of the comparison between the analytic light distribution model and the empiric light distribution model.

5.5. Comparison with literature

In literature several reports have approached the light distribution within a spherical cavity as an integrating sphere, which yields a Lambertian surface. These models were even linked to β.[25,29,39] There are also reports about the light distribution in more complex cavities i.e. ellipsoids.[40] However no data was found on simulating light distribution within a more complex cavity in which the wall reflects light according to lamberts law of diffuse reflection. This research is therefore new in that it simulates the light distribution within a complex geometry of which its wall reflects light according to lamberts law of diffuse reflection.

In literature β is a fixed value which is calculated per cavity.[25,29,33] We found variances in these β's for multiple measurement positions within the same cavity. A linear trend was observed by plotting these factors relative to their distances from the light source. This distance dependency of β is therefore a new-found phenomenon.

A correlation between β with the volume and the surface area of the cavity had been examined. There are reports that link the volume and surface area of simple geometries with the light distribution.[40] However, none had assessed the link between β with the volume and surface area of the cavity in a complex geometry as is done in this study.

6. Conclusion

The analytic model can simulate irradiance and fluence rate at the surface of the cavity wall within acceptable margins i.e. +/- 20 mW, therefore it has the potential to support the physician in its decision making on where to position the light source for cPDT. This model can also easily be expanded with the possibility to simulate a micro-lens. The main drawback of this simulation is the fact that R_d is unknown. Further research should focus on a standard R_d for sinonasal cavities or obtaining R_d fiber optically to make this model clinically viable. R_d can also be estimated but it is unclear whether this gives reliable results. Fitting R_d requires measurements to be conducted in advance including a CT scan during those measurement, which is clinically unpractical.

The empiric light distribution model simulates fluence rates comparable to the fluence rates measured. It can only be concluded that the simulation with the use of $\beta(r)$ works well if the light source is located near the light source location used in the measurement. It remains questionable whether the method is valid in case the location of the light source is further away from the light source location used in the measurements. Also, application in clinical practice would result in fluctuations in $\beta(r)$ due to the limited number of measuring probes that can be used. It remains questionable how much the fluctuation in $\beta(r)$ influences the simulated fluence. Finally, the influence on the type of $\beta(r)$ needs further analysis as well as the model's validity at close distances.

The research question was what light distribution model could be used for a planning soft-ware which determines optimal source location(s) based on physical calculations. Both models show acceptable simulations within the conducted phantom measurements. Regarding the clinically applicability and the calculation speed it seems that the empiric model is more clinically applicable than the analytic model, however more research is needed to give a definitive conclusion on this.

7. Future work suggestions

7.1. Analytic model

To technically improve the analytic model the first step would be implementing the same mathematics in a leaner and faster coding language to improve the calculating capacity. This larger capacity will make it possible to do the same calculations for a more detailed cavity, what will likely reduce the error made per calculated reflection as is discussed.

Once this is possible it can even be considered to change the raytracing technique into a more sophisticated raytracing technique in which more rays are simulated. A combination can be made with the ray-triangle intersection method described by Möller et. al.[41] This way, a face can have multiple degrees of shadow fall instead of one third steps.

A way to extend the model is by adding the feature to skew the Lambertian backscattering profile with the use of the angle of incidence. Xia et al. found that isotropic tissue had a backscattering profile that approached a Lambertian distribution under normal incidence of light. When an oblique light incidence was applied a skewed Lambertian reflection distribution was observed.[30] An easier first step would be to add specular reflection instead of skewing the Lambertian backscattering profile.

Another way to extend the abilities of this model is by adding the ability to simulate a micro-lens. To accomplish this only the calculation of the initial light must be changed as the reflection of the cavity wall remains the same, thus the same calculations can be performed for each successive reflection.

The system assumes a homogeneous wall, but this wall is not homogeneous in practice. A heterogeneous wall could be considered implementing in the simulation in case a one standard R_d is not sufficient to simulate the light distribution within a cavity. A good step towards a heterogeneous wall would be to distinct bear bone and tissue as bone reflects light more and tissue scatters light more. As far as we can judge at the moment, this is still future speculations.

7.2. Empiric model

The first step to finally be able to conclude which model is the most feasible model is to test how much probes could be used in an in-vivo measurement. A device could be made which enables the user to easily maneuver a light source and multiple measuring probes into the sinonasal cavity. These measuring probes should all have a known fixed distance to determine the cavity's specific $\beta(r)$. Then the accuracy and reliability of these measurements should be determined as the slope of $\beta(r)$ can fluctuate due to usage of a limited amount of measuring probes.

The influence on greater light source shifting could be further examined in case of a linear dependent $\beta(r)$. Figure 31 suggests that $\beta(r)$ is slightly shifted when changing the position of the light source. Earlier studies suggest also a change in β due to light source displacement within a cavity with lower β's and it remains unclear whether the distance dependent $\beta(r)$ also changes due to light source shiftment.[33]

The empiric model is built around a linear dependent $\beta(r)$. This is an assumption and it is still unclear whether this function is indeed a linear function. In case of the measurements performed in this study a linear approach seemed to be a reasonable approach. Further research could focus on the possibility that $\beta(r)$ can be a higher order function. It should be kept in mind that the goal is to create a simple light distribution model which can be used to optimize light source position and thus possesses a short

computation time. Higher order functions will probably increase the computation time, question remains how much this will be. More interesting would be to assess the assumption that the linear function goes through point (0,1). This assumption has been made by logical reasoning, but there is no hard evidence for it.

7.3. Measurements

The measurements are performed in 3DPPs and in a TP. These phantoms all have a homogeneous wall whose optical property remains the same over the entire wall. In these measurements, it is therefore not considered that the optical properties can vary on the wall in practice. Phantom measurements can be done to determine the effect on light distribution within a cavity with a wall that has varying optical properties. At the moment it is not yet possible to say whether both models work in such a situation.

Accurate measurements within patients are essential for validation of the simulation models. We have performed these measurements but are put in the appendix because these were not as accurate as we hoped they would be. The main issue and thus the main improvement points are to navigate the measuring probes and light source without too much instruments. The nasal cavity allows passage only for a limited number of tools. The best way is to make the light source and measuring probes navigated so that no extra navigation tool is needed. Another option would be to include patients without a hard palate, this way the cavity is more accessible which allows the use of more tools.

8. Appendix

8.1. Development of analytic model

The first step in the creation of the analytic model was to create a reflection model which could be used to simulate light distribution within a sphere for first a spherical light diffusor and then for a micro-lens. The sphere represented a simplified sinonasal cavity, which made it possible to create a light reflection model without the need of a raytracing algorithm, hence there are no shadow areas within a perfectly round sphere if the light source is placed within that sphere. A spherical cavity also made prediction and interpretation of the light distribution easier than when a complex geometry was used.

8.1.1. Spherical diffusor in sphere

A digital sphere was made which was given a radius of three centimeters which is comparable to the radius of a sinonasal cavity. The sphere was made of 1000 subareas which all were assumed to absorb a portion of light $(1 - R_d)$ and emit the other portion R_d back into the cavity according to a Lambertian distribution. The assumption of this Lambertian distribution is justified and used by multiple studies.[29–31] The Lambertian distribution has been worked out in more detail in the background.

A reflection model was made for a spherical diffusor, based on the diffuse reflectance model without the specular aspect described in 'Image Based Measurement Systems: Object Recognition and Parameter Estimation' by F. van der Heijden.[32] The calculations are elaborated in the methods.

The first simulation focusses on the effect of the number of reflections simulated for multiple measuring points on the surface of the spherical cavity. The simulated fluence rates of three positions on the sphere are plotted in the graph below.

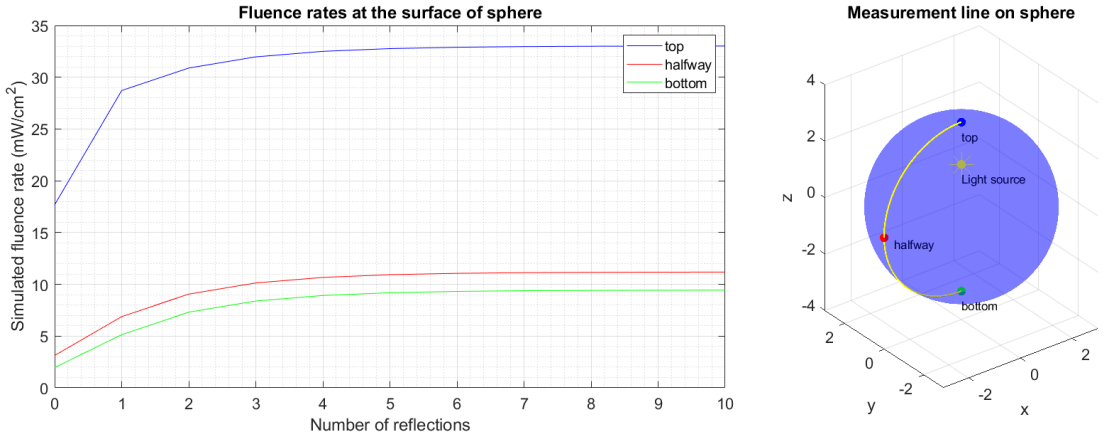

Figure 37 - On the left are the fluence rates at the surface of sphere plotted and, on the right, the spherical cavity is visualized together with the light source and measuring points. A light distribution simulation is performed in a sphere with a radius of 3 cm and a R_d of 0.5. The light source i.e. spherical diffusor is located at the location (0,0,1.5) within the sphere.

This graph shows that after a certain number of reflections e.g. 7 the simulated fluence rate does not change significantly. All three the positions show the same trend and plateau at the same number of reflections simulated. Thus, the location of the measuring point on the sphere surface does not affect the number of reflections needed, they all plateau at approximately the same number of reflections.

Then the influence of R_d on the simulated fluence rate was assessed by changing R_d and plotting the simulated fluence rates per number of reflections simulated. The result of this simulation is plotted in the figure below.

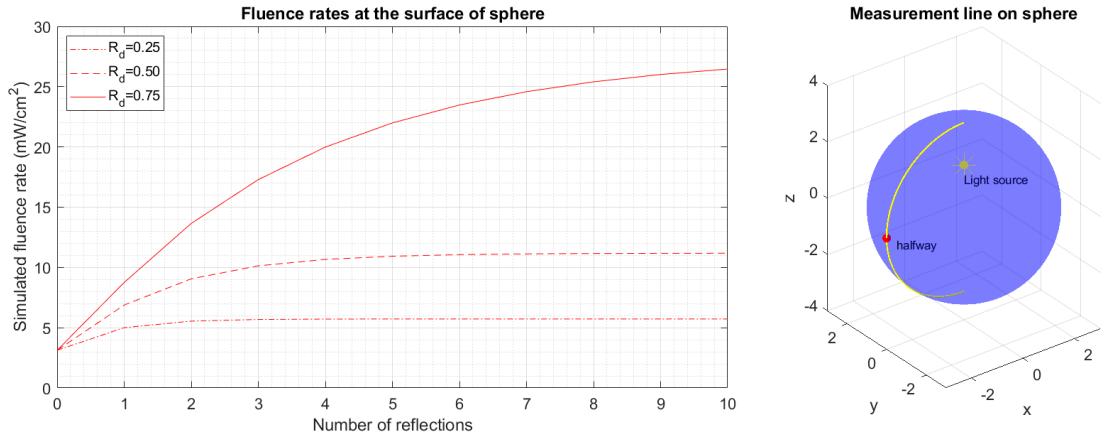

Figure 38 - Fluence rates at the surface of sphere at point 'halfway'. Three simulations are performed within a sphere with a radius of 3 cm and changing R_d i.e. 0.25, 0.50 and 0.75. The light source i.e. spherical diffusor is located at the location (0,0,1.5) within the sphere. From this graph a larger number of reflections needs to be simulated for a higher value of R_d until the simulated fluence rate does not change anymore.

This graph shows that a higher value of R_d results in a larger number of reflections needed until the simulated fluence rates reaches a plateau. The simulated fluence rates in case of a low R_d need only a small number of simulations before a plateau is reached. Thus R_d does affect the number of reflections needed.

The next step was to assess the influence of light source displacement within the sphere. Multiple simulations were made, changing the light source position in the z-direction. The simulated fluence rates of three positions on the sphere are plotted against the z-coordinate of the light source in the graph below.

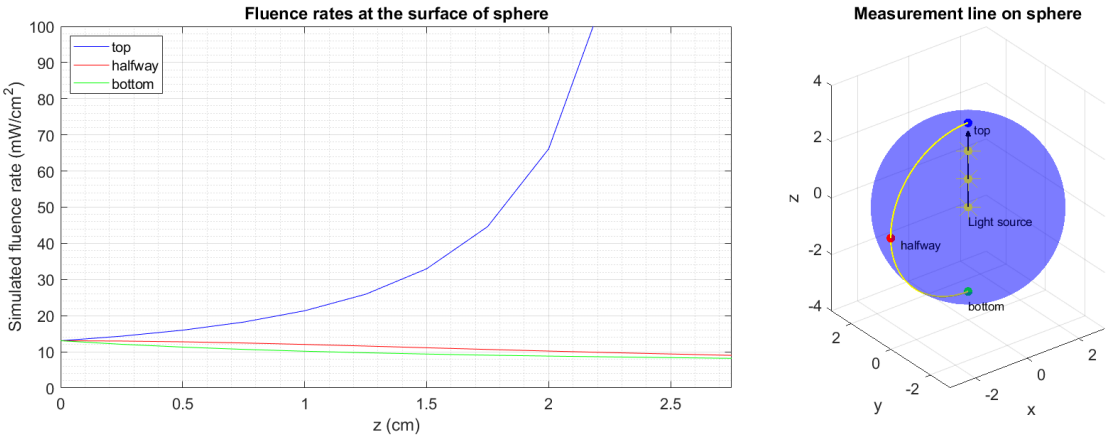

Figure 39 - The influence of light source displacement. The light source has been moved in the z-direction. The simulated fluence rate is plotted against z-coordinate of the light source. The simulations are performed in a sphere with a radius of 3cm. The R_d is set at 0.5 and 7 reflections are simulated, because it is assumed that after 7 reflections the simulated fluence rate does not change significantly (Figure 37).

This graph shows that the placement of the light source within a spherical cavity influences the light distribution. It is therefore useful to plan the location of the light source in order to achieve a good light distribution.

8.1.2.Micro-lens in sphere

The reflection model was modified so that it can simulate the light distribution for a micro-lens. The modification concerned only the direct initial light simulated, because the properties of the cavity are unchanged and therefore the same calculations can be performed for each reflection. The direct initial light of the micro-lens is now calculated according to the properties of the micro-lens which are schematically drawn in Figure 6. The lens generates a homogeneous spot with an angular aperture of (34.7°) and the direct initial fluence rate can therefore be calculated with equation (2).

A simulation is performed for a micro-lens in which the effect of the number of reflections on the fluence rate is assessed. The simulated fluence rates of three positions on the sphere are plotted against the number of simulations in the graphs below.

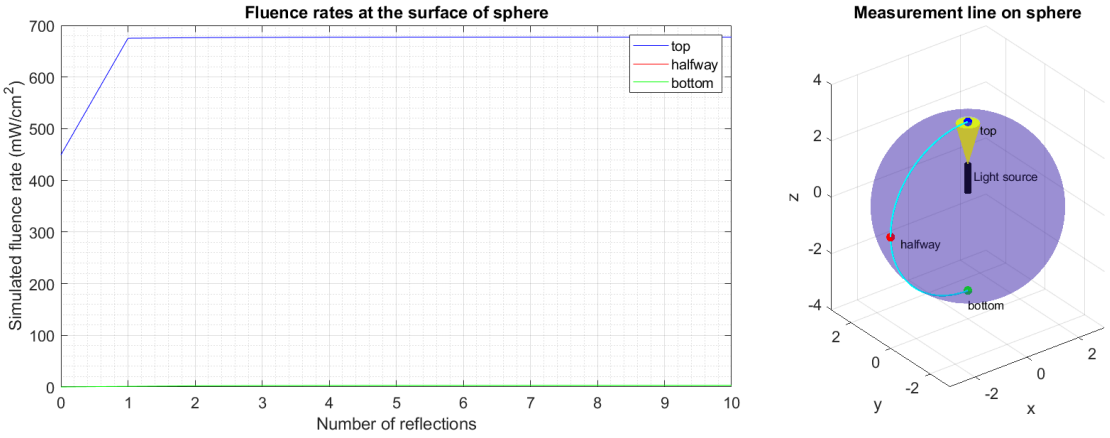

Figure 40 - Fluence rates at the surface of the sphere in case of a micro-lens. The fluence rates are plotted against the number of reflections simulated and in the right figure the sphere is visualized together with the micro-lens and the measuring points. A light distribution simulation is performed in a sphere with a radius of 3 cm and a R_d of 0.5. The light source i.e. micro-lens is located at the location (0,0,1.5) within the sphere.

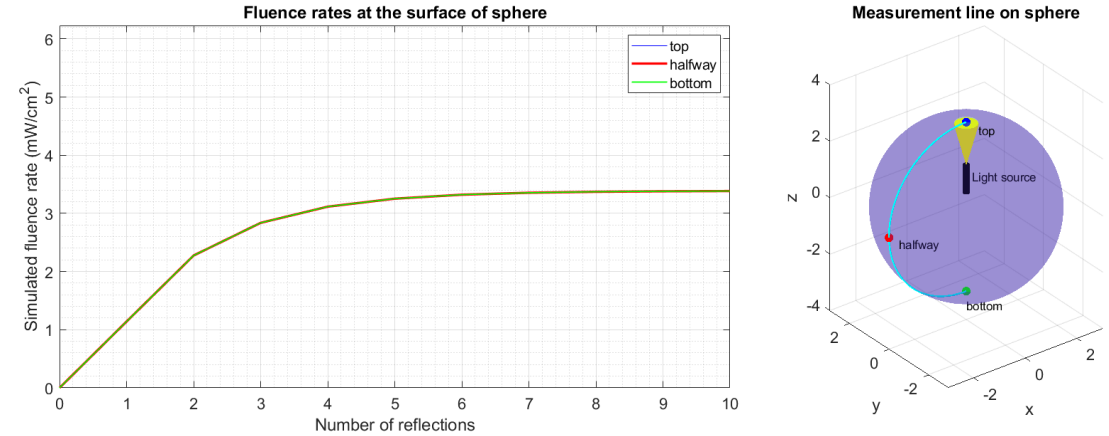

Figure 41 - This is the same as figure 40, but the range of the 'simulated fluence rate'-axis is lowered to show the curve of 'halfway' and 'bottom' measuring points.

From the graphs above it can be concluded that the fluence rate in the spot is significantly higher than the fluence rate outside the spot on the wall of a spherical cavity. A closer look at the points 'halfway' and 'bottom' show that the fluence rates of these two points are approximately the same. This is what is expected within a perfect spherical cavity that reflects light according to Lamberts law of diffuse reflection.

8.2. Patient measurement

The fluence rate measurements in the patients were conducted in a similar fashion as the 3DPPs. What was different was that these dosimetry measurements were performed in human patients, therefore obtaining spatial information of the light source and probe positions was done with the Medtronic EM-navigation system. This system needed a planning CT of the head and neck area on which predetermined light source positions were marked. In this measurement just one isotropic probe (navigated) was used to measure the fluence rate, because the narrow passage to the sinonasal cavity allowed the use of a limited number of instruments i.e. isotropic probe, light source, endoscope and navigation tools.

First the light source was guided to the predetermined position with the use of the planning CT and the navigation system. Once the light source was positioned it was fixated with a surgical fixation arm, allowing to use the navigation tool to place the isotropic probe. The isotropic probe was manually kept in place during measurement.

The measurement was also simulated with both light distribution models. R_d was estimated to be 0.6, thus 10 reflections are simulated, since after 10 reflections the amount of light is below 1% of the light emitted by the light source ($P_{out}0.60^{10} = P_{out}0.006$). The results of the measurements and simulations are visualized in the table below.

Source location	Detector nr.	Measured fluence rate (mW/cm^2)	Distance (cm)	Analytic simulation (mW/cm^2)	Empiric simulation (mW/cm^2)
1	1	15.0	3.24	36.2	40.5
1	2	25.2	3.23	27.0	40.6
2	1	79.8	2.01	67.4	74.3
2	2	80.3	1.77	151.0	88.6

Table 8 - Patient measurement and simulations.

R_d is not manually fitted as is done for the tissue and 3DPPs because there are only two measuring probes used for the measurement and the placement of these measuring probes are not accurate.

The measurements done in the first patient was affected by multiple inaccuracies, which make it questionable whether these measurements are usable. The inaccuracies where caused by e.g. missing fixation arm for the light source, movement of the measuring probe during measurement and the fact that the measuring probe was not fixated on the navigation tool.

In the measurements the measurement probes were placed near the surface of the cavity wall, but there was still a reasonable distance between the measuring probe and the cavity wall. The analytic simulation can only simulate the fluence rate on the surface and not in mid-air what the measuring probes were measuring. That is why a reasonable difference has arisen between the simulated value and the measured value.

9. Bibliography

1. Nederlandse Vereniging voor KNO. Dutch Guidelines Head-neck cancer. 2014:1-228. https://www.nvmka.nl/sites/www.nvmka.nl/files/Richtlijn Hoofd-halstumoren 2015.pdf.
2. Integraal kankercentrum Nederland (IKNL). Cijfers over kanker. 2018. https://www.cijfersoverkanker.nl/selecties/Dataset_1/img5c1b7c932c025.
3. Karakullukçu MB. New Insights into Photodynamic Therapy of the Head and Neck New Insights into Photodynamic Therapy of the Head and Neck. 2014. http://hdl.handle.net/11245/1.409799.
4. D'Cruz AK, Robinson MH, Biel MA. mTHPC-mediated photodynamic therapy in patients with advanced, incurable head and neck cancer: a multicenter study of 128 patients. *Head Neck*. 2004;26(3):232-240. doi:10.1002/hed.10372.
5. O'Connor AE, Gallagher WM, Byrne AT. Porphyrin and nonporphyrin photosensitizers in oncology: Preclinical and clinical advances in photodynamic therapy. *Photochem Photobiol*. 2009;85(5):1053-1074. doi:10.1111/j.1751-1097.2009.00585.x.
6. van Doeveren TEMM, Karakullukçu MB, van Veen RLPP, Lopez-Yurda M, Schreuder WH, Tan IB. Adjuvant photodynamic therapy in head and neck cancer after tumor-positive resection margins. *Laryngoscope*. 2018;128(3):657-663. doi:10.1002/lary.26792.
7. Agostinis P, Berg K, Cengel K. KA, et al. Photodynamic Terapy of cancer: an update. *CA Cancer J Clin*. 2011;61(4):250-281. doi:10.3322/caac.20114.PHOTODYNAMIC.
8. Caesar L, Doeveren TEM Van, Tan IB, et al. The use of photodynamic therapy as adjuvant therapy to surgery in recurrent malignant tumors of the paranasal sinuses. *Photodiagnosis Photodyn Ther*. 2015;12(3):414-421. doi:https://doi.org/10.1016/j.pdpdt.2015.06.001.
9. Allison RR, Moghissi K. Photodynamic therapy (PDT): PDT mechanisms. *Clin Endosc*. 2013;46(1):24-29. doi:10.5946/ce.2013.46.1.24.
10. Dolmans DEJGJ, Fukumura D, Jain RK. Photodynamic therapy for cancer. *Nat Rev Cancer*. 2003;3:380-387. doi:10.1038/nrc1070.
11. Kwiatkowski S, Knap B, Przystupski D, et al. Photodynamic therapy – mechanisms, photosensitizers and combinations. *Biomed Pharmacother*. 2018;106(June):1098-1107. doi:10.1016/j.biopha.2018.07.049.
12. Ahn PH, Finlay JC, Gallagher-colombo SM, et al. Lesion oxygenation associates with clinical outcomes in premalignant and early stage head and neck tumors treated on a phase 1 trial of photodynamic therapy. *Photodiagnosis Photodyn Ther*. 2018;21(November 2017):28-35. doi:10.1016/j.pdpdt.2017.10.015.
13. Civantos FJ, Karakullukcu B, Biel M, et al. A Review of Photodynamic Therapy for Neoplasms of the Head and Neck. *Adv Ther*. 2018;35(3):324-340. doi:10.1007/s12325-018-0659-3.
14. Sterenborg HJCM, Van Veen R, Aans J-B, et al. Light Dosimetry for Photodynamic Therapy: Basic Concepts. 2013;(November 2014):281-291.
15. Penjweini R, Kim MM, Finlay JC, Zhu TC. Investigating the impact of oxygen concentration and blood flow variation on photodynamic therapy. In: Vol 9694. ; 2016:96940L-9694-7. doi:10.1117/12.2211120.Investigating.
16. Zhu TC, Kim MM, Ong Y-H, et al. A summary of light dose distribution using an IR navigation system for Photofrin-mediated Pleural PDT. *Prog Biomed Opt Imaging - Proc SPIE*. 2017;10047. doi:10.1117/12.2253027.
17. R.v.Veen. *In Vivo Optical Measurements for Diagnostics and Monitoring of Treatment*.; 2006.
18. Betrouni N, Munck C, Bensoltana W, et al. Real-time light dosimetry for intra-cavity photodynamic therapy: Application for pleural mesothelioma treatment. *Photodiagnosis Photodyn Ther*. 2017;18:155-161. doi:10.1016/j.pdpdt.2017.02.011.

19. Henderson BW, Busch TM, Snyder JW. Fluence rate as a modulator of PDT mechanisms. *Lasers Surg Med*. 2006;38(5):489-493. doi:10.1002/lsm.20327.
20. Ong YH, Finlay J, Kim M, et al. Determination of optical properties, drug concentration and tissue oxygenation in human pleural tissue before and after Photofrin-mediated photodynamic therapy. In: *Proceedings of SPIE--the International Society for Optical Engineering*. Vol 10476. ; 2018:34. doi:10.1117/12.2290727.
21. Yoon I, Li JZ, Shim YK. Advance in photosensitizers and light delivery for photodynamic therapy. *Clin Endosc*. 2013;46(1):7-23. doi:10.5946/ce.2013.46.1.7.
22. Zhu C, Liu Q. Review of Monte Carlo modeling of light transport in tissues. *J Biomed Opt*. 2013;18(5):050902. doi:10.1117/1.JBO.18.5.050902.
23. Dupont C, Vignion A-S, Mordon S, Reyns N, Vermandel M. Photodynamic therapy for glioblastoma: A preliminary approach for practical application of light propagation models. *Lasers Surg Med*. 2017;(August). doi:10.1002/lsm.22739.
24. Mang TS. Lasers and light sources for PDT: Past, present and future. *Photodiagnosis Photodyn Ther*. 2004;1(1):43-48. doi:10.1016/S1572-1000(04)00012-2.
25. Sandell JL, Zhu TC. A review of in-vivo optical properties of human tissues and its impact on PDT. *J Biophotonics*. 2011;4(11-12):773-787. doi:10.1002/jbio.201100062.
26. Dai T, Fuchs BB, Coleman JJ, et al. Concepts and principles of photodynamic therapy as an alternative antifungal discovery platform. *Front Microbiol*. 2012;3(APR):1-16. doi:10.3389/fmicb.2012.00120.
27. Baskaran R, Lee J, Yang S-G. Clinical development of photodynamic agents and therapeutic applications. *Biomater Res*. 2018;22(25):1-8. doi:10.1186/s40824-018-0140-z.
28. Benaron DA, Cheong W-F, Stevenson DK. Tissue Optics. *Science (80-)*. 1997;276(5321):2002-2003. doi:10.1126/science.276.5321.2002.
29. Star WM. The relationship between integrating sphere and diffusion theory calculations of fluence rate at the wall of a spherical cavity. *Phys Med Biol*. 1995;40(1):1. http://stacks.iop.org/0031-9155/40/i=1/a=001.
30. Xia J, Yao G. Angular distribution of diffuse reflectance in biological tissue. *Appl Opt*. 2007;46(26):6552-6560. doi:10.1364/AO.46.006552.
31. Timothy C. Zhu, Andreea Dimofte, Stephen M. Hahn RAL. Light dosimetry at tissue surfaces for small circular fields. *Proc SPIE--the Int Soc Opt Eng*. 2003;4952:4952-4952. doi:10.1117/12.474144.
32. Heijden F van der. *Image Based Measurement Systems: Object Recognition and Parameter Estimation*.; 1994.
33. Staverent HJ Van, Beeu JF, Ramaekerst JWH, Star WM, Star HJ van S and JFB and JWHR and MK and WM. Integrating sphere effect in whole bladder wall photodynamic therapy. I. 532 nm versus 630 nm optical irradiation. *Phys Med Biol*. 1994;39(6):947. http://stacks.iop.org/0031-9155/39/i=6/a=003.
34. Koning SGB de, Baltussen EJM, Karakullukcu MB, et al. Toward complete oral cavity cancer resection using a handheld diffuse reflectance spectroscopy probe. 2018;23:121611-121618. https://doi.org/10.1117/1.JBO.23.12.121611.
35. Marijnissen JPA, Star WM. Calibration of isotropic light dosimetry probes based on scattering bulbs in clear media. *Phys Med Biol*. 1996;41(7):1191. http://stacks.iop.org/0031-9155/41/i=7/a=008.
36. Star WM. Light dosimetry in vivo. *Phys Med Biol*. 1997;42(5):763-787. doi:10.1088/0031-9155/42/5/003.
37. Hecht HG. The Interpretation of Diffuse Reflectance Spectra. *J Res Natl Bur Stand A*. 1976;80(4):567-583. doi:10.6028/jres.080A.056.

38. Dam JS, Andersen PE, Dalgaard T, Fabricius PE. Determination of tissue optical properties from diffuse reflectance profiles by multivariate calibration. *Appl Opt*. 1998;37(4):772. doi:10.1364/AO.37.000772.
39. Sandell J, Chang C, Finlay JC, Zhu TC. A treatment planning system for pleural PDT. In: Vol 7551. ; 2010:75510C-7551-6. doi:10.1117/12.843044.A.
40. Zhu T, Kim M, Padawer J, et al. Light Fluence Dosimetry in Lung-simulating Cavities. In: *Proceedings of SPIE--the International Society for Optical Engineering*. Vol 10476. ; 2018:14. doi:10.1117/12.2291355.
41. Moller T, Trumbore B. Fast, minimum storage ray-triangle intersection. *Doktorsavhandlingar vid Chalmers Tek Hogsk*. 1998;(1425):109-115. doi:10.1080/10867651.1997.10487468.